

Horizons in a binary black hole merger II: Fluxes, multipole moments and stability

Daniel Pook-Kolb,^{1,2} Ofek Birnholtz,³ José Luis Jaramillo,⁴ Badri Krishnan,^{1,2} and Erik Schnetter^{5,6,7}

¹*Max-Planck-Institut für Gravitationsphysik (Albert Einstein Institute), Callinstr. 38, 30167 Hannover, Germany*

²*Leibniz Universität Hannover, 30167 Hannover, Germany*

³*Department of Physics, Bar-Ilan University, Ramat-Gan 5290002, Israel*

⁴*Institut de Mathématiques de Bourgogne (IMB), UMR 5584, CNRS, Université de Bourgogne Franche-Comté, F-21000 Dijon, France*

⁵*Perimeter Institute for Theoretical Physics, Waterloo, ON N2L 2Y5, Canada*

⁶*Physics & Astronomy Department, University of Waterloo, Waterloo, ON N2L 3G1, Canada*

⁷*Center for Computation & Technology, Louisiana State University, Baton Rouge, LA 70803, USA*

We study in detail the dynamics and stability of marginally trapped surfaces during a binary black hole merger. This is the second in a two-part study. The first part studied the basic geometric aspects of the world tubes traced out by the marginal surfaces and the status of the area increase law. Here we continue and study the dynamics of the horizons during the merger, again for the head-on collision of two non-spinning black holes. In particular we follow the spectrum of the stability operator during the course of the merger for all the horizons present in the problem and implement systematic spectrum statistics for its analysis. We also study more physical aspects of the merger, namely the fluxes of energy which cross the horizon and cause the area to change. We construct a natural coordinate system on the horizon and decompose the various fields appearing in the flux, primarily the shear of the outgoing null normal, in spin weighted spherical harmonics. For each of the modes we extract the decay rates as the final black hole approaches equilibrium. The late part of the decay is consistent with the expected quasi-normal mode frequencies, while the early part displays a much steeper fall-off. Similarly, we calculate the decay of the horizon multipole moments, again finding two different regimes. Finally, seeking an explanation for this behavior, motivated by the membrane paradigm interpretation, we attempt to identify the different dynamical timescales of the area increase. This leads to the definition of a “slowness parameter” for predicting the onset of transition from a faster to a slower decay.

I. INTRODUCTION

In classical general relativity, black holes are perfect absorbers. They grow inexorably by absorbing matter and/or radiation from their surroundings. Emission of electromagnetic or gravitational radiation occurs due to interactions of the black hole with surrounding spacetime or matter. Gravitational waves are emitted due to non-stationarities and non-linearities of the spacetime metric in the region around the black hole. Black holes have an additional special feature which does not hold for other physical objects, namely a very special set of equilibrium states determined by only two parameters in astrophysical contexts. In other words, astrophysical black holes within standard general relativity have no hair. Normal physical objects reach equilibrium by both absorbing and emitting, but black holes do not have that luxury. Not only must they only absorb, but they must absorb very selectively so that the absorbed radiation precisely cancels any hair it might initially have.

This picture applies to a binary black hole merger. When the final remnant black hole is initially formed, its horizon is highly distorted but its final state is that of a simple Kerr black hole. This process of reaching equilibrium from its initial state at formation must follow the process of selective absorption mentioned above. This process of reaching equilibrium is often referred to as the black hole “radiating away its hair”. This is accurate when one considers a sufficiently large spacetime region

containing the black hole; after all, it is not just the horizon that reaches equilibrium, but rather the spacetime itself in a neighborhood of the horizon. However, “radiating away hair” is not an apt description for the horizon itself in classical general relativity.

The issue of how a black hole knows precisely how much radiation to absorb at any given time, is an important one in general relativity. From a mathematical perspective, it touches on the question of the stability of the Kerr black hole in full non-linear general relativity. From a theoretical physics viewpoint, any deviations of the final state from Kerr might indicate support for alternate theories of gravity. As we have argued in the previous paragraph, this issue of the final state is intimately connected with the in-falling energy flux through the horizon. One important goal of analytic or theoretical studies is thus to discover universalities in the approach to equilibrium of a black hole horizon in full non-linear general relativity. These universalities might be reflected in the rates of exponential or power-law decay. Gravitational wave observations of binary black hole mergers offer opportunities for testing these predictions observationally.

A useful way of approaching these problems is via the study of marginally trapped surfaces. These are special spherical surfaces for which outgoing light rays have vanishing convergence. These surfaces are well suited for describing not only stationary black holes, but also binary mergers and other dynamical processes involving black holes. The entire process of merger and approach to equi-

librium can be understood in terms of marginally trapped surfaces. Recent numerical studies have discovered new geometric and topological features of marginally trapped surfaces in binary black hole mergers. These include their behavior under time evolution, the status of the area increase law, and the presence of topological features such as cusps and knots. These numerical results rely on a new method for locating marginally outer trapped surfaces [1, 2], and the physical results are based on the formalism of quasi-local horizons. This formalism is based on the world tube of marginally trapped surfaces and it provides a coherent way of studying various aspects of black hole physics quasi-locally [3–9]. For our purposes, it is important that there exist exact flux formulae for these horizons within full general relativity, which quantify the amount of energy and radiation crossing the horizon, and relate it to the change in horizon area [10, 11]. The flux due to gravitational radiation is positive definite and always causes the area to increase. This is analogous to the well known Bondi mass-loss formula at null infinity in the Bondi-Sachs framework describing the energy carried away by gravitational radiation.

It turns out that in these astrophysical situations, the fluxes falling through the horizon are highly correlated with the fluxes at infinity which can be observed by gravitational wave detectors [12–16]. This might appear surprising at first glance since the horizons are causally disconnected from observers outside the event horizon. However, in these astrophysical situations the source of the infalling radiation and the outgoing radiation are one and the same, namely non-linearities and non-stationarities in the spacetime region near (but outside) the black holes. Thus, a better understanding of the horizon fluxes might help us to quantify these correlations better. Eventually, one might be able to observationally infer properties of spacetime regions hidden behind event horizons.

The goal of this paper is to study, via numerical simulations, horizon fluxes in binary black hole mergers, and the approach to equilibrium. The basic scenario outlining how marginally trapped surfaces merge has been established in [1, 2]. The present series of papers follows up on these results by studying physical and geometrical properties of marginally trapped surfaces and their time evolution. The first paper (henceforth paper I) has studied basic properties of these world tubes including their signature and the status of the area increase law. The goal here is to study in detail physical aspects of these world tubes. These include energy fluxes across the world tubes, their decay rates as the final black hole approaches equilibrium, the evolution of the horizon multipole moments, and their stability properties. While we often refer to paper I (and the reader might benefit by having a copy of that paper at hand), this paper is meant to be mostly self-contained.

The plan for the rest of this paper is as follows. Sec. II sets up notation and briefly summarizes some of the basic notions and results that we shall use later. Paper I has already summarized the main definitions and con-

cepts of quasi-local horizons that we employ. Here we shall summarize results pertaining to the horizon fluxes, the stability operator and the multipole moments. Especially important will be the construction of an invariant coordinate system on the horizon which will be used to decompose various fields on the horizon. Sec. III discusses the stability of the various MOTSs. The stability here refers to the properties of a MOTS under small outward deformations, and is governed by an elliptic operator. The horizon will be stable if this operator is invertible, i.e. when its spectrum does not contain zero. This leads us then to analyze the spectral properties of the operator, yielding what might be called the stability spectrum of the MOTS and pushing forward the study of the full MOTS-spectral problem formulated in [17–19] in particular introducing a discussion in terms of spectrum statistics.

Sec. IV addresses the question of why the area changes, namely due to the flux of gravitational radiation across the horizon. The most important part of the radiation flux is the shear which, just like the gravitational radiation observed by gravitational wave detectors, is a symmetric tracefree tensor, except that it lives on the horizon. The horizon, being a non-null surface, also has another contribution to the flux from a vector field on the horizon. We study the multipolar decomposition of both of these contributions. We then connect the decay rate of the flux to the quasi-normal mode frequencies associated with the final black hole. Sec. V presents the evolution of the horizon multipole moments. The multipole moments capture the deviation of the horizon from a simple Schwarzschild geometry (or Kerr, if the black holes had been rotating). Thus, the evolution of the multipole moments in time tells us about how the two individual black holes become increasingly distorted, and how the final black hole approaches equilibrium. This is, of course closely connected with the fluxes discussed in Sec. IV. Sec. VI offers a tentative explanation for why we have two regimes in the approach to equilibrium. It shows that the non-linear effects dominate in the steep decay regime at early times, while the later time is consistent with linear behavior. Sec. VII concludes by discussing open questions and possible directions for future work. The mathematical issues discussed in Sec. III (namely spectral theory) are quite different from the topics of Secs. IV and V (fluxes, multipole moments, quasi-normal modes, and non-linearities); they can thus be read quite independently of each other.

II. BASIC NOTIONS

A. Marginally trapped surfaces and dynamical horizons

The basic notions of marginally trapped surfaces and dynamical horizons were already summarized in paper I. Several review articles on the subject are also available

[3–5, 7–9]. We shall therefore be very brief with the basic definitions. The focus will be on the flux laws, multipole moments and the stability operator.

Let spacetime be modeled as a 4-dimensional manifold \mathcal{M} equipped with a Lorentzian metric g_{ab} with signature $(-, +, +, +)$. We shall only consider vacuum spacetimes. Let ∇_a be the derivative operator compatible with g_{ab} . Let \mathcal{S} be a closed 2-dimensional spacelike manifold immersed in \mathcal{M} . \mathcal{S} is taken to be orientable and of spherical topology. Let \tilde{q}_{ab} , $\tilde{\epsilon}$, and \mathcal{D}_a be the intrinsic Riemannian metric on \mathcal{S} , the volume 2-form, and the corresponding derivative operator, respectively. The intrinsic scalar curvature of \mathcal{S} will be denoted \mathcal{R} , its area $A_{\mathcal{S}}$, and the Laplacian on \mathcal{S} is $\Delta_{\mathcal{S}}$.

The outgoing and ingoing future directed null-normals to \mathcal{S} will be denoted by ℓ^a and n^a respectively. We will tie the normalizations of the null normals together by requiring $\ell \cdot n = -1$. Finally, given a complex null vector m^a tangent to \mathcal{S} satisfying $m \cdot \bar{m} = 1$, we obtain a null-tetrad (ℓ, n, m, \bar{m}) .

The expansions $\Theta_{(\ell)}$ and $\Theta_{(n)}$ of ℓ^a and n^a are respectively

$$\Theta_{(\ell)} = \tilde{q}^{ab} \nabla_a \ell_b, \quad \Theta_{(n)} = \tilde{q}^{ab} \nabla_a n_b. \quad (1)$$

The shears $\sigma_{(\ell)}$ and $\sigma_{(n)}$ of ℓ^a and n^a , respectively, are

$$\sigma_{(\ell)} = m^a m^b \nabla_a \ell_b, \quad \sigma_{(n)} = m^a m^b \nabla_a n_b. \quad (2)$$

We shall usually not need $\sigma_{(n)}$ in this paper, and thus we shall often refer to $\sigma_{(\ell)}$ just as the shear σ .

The other important field is the connection 1-form on the normal bundle of \mathcal{S} :

$$\omega_a = -n_b q_a^c \nabla_c \ell^b. \quad (3)$$

It can be shown that ω_a relates to the angular momentum associated with \mathcal{S} (see e.g. [11, 20]). In this paper we consider only non-spinning black holes. Thus while we will occasionally mention ω_a where appropriate, all of our results have $\omega_a = 0$.

\mathcal{S} is said to be a *future-marginally-outer-trapped* surface if $\Theta_{(\ell)} = 0$ and $\Theta_{(n)} < 0$. If $\Theta_{(n)} > 0$, then \mathcal{S} is said to be *past-marginally-outer-trapped*. A surface satisfying only $\Theta_{(\ell)} = 0$ with no restriction on $\Theta_{(n)}$ is called a marginally outer trapped surface, or MOTS in short.

It is clear that a MOTS is a geometric concept in a spacetime, and makes no reference to any spacelike Cauchy surfaces or time coordinate. Nevertheless, one can think of a Cauchy surface as a convenient means of locating a MOTS: They can be located on a spacelike Cauchy surface Σ equipped with a 3-metric and extrinsic curvature, and well known numerical methods exist for this. The canonical choice of null normals for \mathcal{S} immersed in Σ is

$$\ell^a = \frac{1}{\sqrt{2}} (T^a + R^a), \quad n^a = \frac{1}{\sqrt{2}} (T^a - R^a). \quad (4)$$

Here R^a is the unit spacelike normal to \mathcal{S} (and tangent to Σ), while T^a is the unit timelike normal to Σ . We use

a numerical method recently developed in [1, 2], capable of locating highly distorted surfaces; our implementation is available at [21]. This method is an extension of the widely used method developed in [22–26]. Our numerical calculation use *Einstein Toolkit* [27, 28]. We use *TwoPunctures* [29] to set up initial conditions and an axisymmetric version of *McLachlan* [30] to solve the Einstein equations, which uses *Kranc* [31, 32] to generate efficient C++ code. Results in this paper are obtained from simulations with spatial resolutions $1/\Delta x = 480$ running until $T_{\max} = 20 \mathcal{M}$ and $1/\Delta x = 60$ running until $T_{\max} = 50 \mathcal{M}$, where $\mathcal{M} := M_{\text{ADM}}/1.3$ is our simulation time unit. For brevity, we will occasionally state simulation times using lowercase $t := T/\mathcal{M}$. Here \mathcal{M} is a suitable mass scale in the problem. Further details of the simulation specific to our problem are detailed in [2].

The initial configuration is the same as that used in paper I and in [2]. We use the Brill-Lindquist construction [33], i.e. the initial data is conformally flat and time symmetric. The initial data has two non-spinning black holes with vanishing linear momentum. The “bare masses” are $m_1 = 0.5$ and $m_2 = 0.8$ with the total ADM mass being $M_{\text{ADM}} = 1.3$. The initial separation d_0 is $d_0/M_{\text{ADM}} = 1$. At the initial time, there are two disjoint horizons \mathcal{S}_1 and \mathcal{S}_2 with \mathcal{S}_2 being the larger one. The common horizon forms at a time $T_{\text{bifurcate}}$ shortly after the simulation starts and splits into inner and outer surfaces, $\mathcal{S}_{\text{inner}}$ and $\mathcal{S}_{\text{outer}}$, respectively. The world tubes of these horizons are shown in Fig. 1 of paper I.

The 3-dimensional world tube traced out by the MOTSs is taken as a bonaafide geometric object in its own right and we attempt to understand its physical and geometric properties. The pioneering work by Hayward [34] was an important step in this direction. Another important aspect is a detailed study of the case when the world tube is null, i.e. just like the stationary Schwarzschild and Kerr solutions, the black hole is not absorbing matter/energy and not increasing in area. This can be viewed as an approximation in suitable physical situations (an excellent approximation in many cases), or as the limiting case asymptotically as the black hole reaches equilibrium. The basic definition of a non-expanding horizon and its extensions to an isolated horizon has been summarized in paper I. A detailed understanding of this case has been achieved and an extensive literature on isolated horizons is available (see e.g. [20, 35–44]). For the dynamical case, we need to consider a general world tube of arbitrary signature which will be called a dynamical horizon. Additional qualifiers such as timelike or spacelike, and future and past (depending on the sign of $\Theta_{(n)}$) will be included as required.

B. Variations and the stability operator

Given a MOTS \mathcal{S} on a Cauchy surface Σ and a choice of lapse and shift, i.e. a time evolution vector, consider the behavior of the MOTS under time evolution. If the

MOTS were to evolve smoothly under this time evolution, it would trace out a smooth 3-dimensional world tube. In the well known stationary solutions, e.g. the Schwarzschild or Kerr black holes, the event horizons are foliated by MOTSs. If the world tube does exist also in fully dynamical situations, then it is possible to formulate black hole physics and thermodynamics in various physical scenarios. Seminal work by Hayward in 1994 introduced the notion of trapping horizons [34] and showed how one could formulate the laws of black hole thermodynamics in this framework for dynamical black holes. Similarly, horizon fluxes were studied in [10, 11] and shown to be manifestly positive definite. In this early work on this topic, it was usually assumed that this smooth world tube exists in full non-linear general relativity. This was a reasonable assumption, especially given the fact that MOTSs were already widely used in numerical relativity for locating and extracting physical black hole parameters [45]. In these numerical simulations the apparent horizons were generally found to evolve smoothly. The mathematical conditions under which a MOTS evolves smoothly were found in 2005 [46–48]. A central role in these proofs is played by the stability operators associated with a MOTS and their eigenvalues, which we now describe.

The starting point here is the notion of the variation of a MOTS [49]. One chooses a vector field X^a along which \mathcal{S} is to be varied, thereby obtaining a family of surfaces \mathcal{S}_λ at least for small values of λ . Starting with a point p on \mathcal{S} , varying λ yields a curve with X^a as the tangent vector at p ; $\mathcal{S}_{\lambda=0}$ is identified with \mathcal{S} itself. Variations tangent to \mathcal{S} do not play an important role here, and we take X^a to be orthogonal to \mathcal{S} . Given this family \mathcal{S}_λ depending smoothly on λ , one can consider *variations* of geometric quantities on \mathcal{S} . For a MOTS, the quantity of interest is the expansion $\Theta_{(\ell)}$. For each \mathcal{S}_λ , we define null normals just as for \mathcal{S} itself. The expansion can be computed for each value of λ and then differentiated. This defines the variation of $\Theta_{(\ell)}$ along X^a , which is denoted $\delta_X \Theta_{(\ell)}$. This is not to be confused with usual derivatives of $\Theta_{(\ell)}$. In particular, $\delta_{\psi X} \Theta_{(\ell)} \neq \psi \delta_X \Theta_{(\ell)}$ when ψ is not a constant. This leads to the definition of the stability operator L acting on functions $\psi : \mathcal{S} \rightarrow \mathbb{R}$ as

$$L^{(X)}[\psi] := \delta_{\psi X} \Theta_{(\ell)}. \quad (5)$$

Since X^a is orthogonal to \mathcal{S} , given a choice of the null normals (ℓ^a, n^a) , we can write

$$X^a = b\ell^a + cn^a, \quad (6)$$

where b and c are functions on \mathcal{S} . We see then that there is not just a single stability operator, but several depending on the normal direction. This is why we label the stability operator $L^{(X)}$ with X .

One case is well known and easy to understand, namely when X^a is along ℓ^a . This should just be the Raychaudhuri equation, and indeed, setting $\Theta_{(\ell)} = 0$ and assuming spacetime to be vacuum leads to

$$L^{(\ell)}[\psi] = \delta_{\psi \ell} \Theta_{(\ell)} = -2|\sigma|^2 \psi. \quad (7)$$

Clearly, if ψ is positive, then this variation will be negative. Moreover, this variation is linear in ψ and does not involve any derivatives. The other component of the variation is along n^a ; it will be convenient to consider the outgoing direction $-n^a$ instead. This turns out to lead to a second order elliptic operator:

$$L^{(-n)}[\psi] = (-\Delta_{\mathcal{S}} + 2\omega^a \mathcal{D}_a) \psi + \left(\frac{1}{2} \mathcal{R} + \mathcal{D}_a \omega^a - \omega^a \omega_a \right) \psi. \quad (8)$$

The presence of the first derivative causes this operator to be non-self-adjoint. We will have $\omega = 0$ in this paper, whence this simplifies to a self-adjoint operator

$$L^{(-n)}[\psi] = \left(-\Delta_{\mathcal{S}} + \frac{1}{2} \mathcal{R} \right) \psi. \quad (9)$$

We have seen that the variation along ℓ^a is “negative”. On the other hand, since $-\Delta_{\mathcal{S}}$ has positive eigenvalues, the variation along $-n^a$ is seen to be positive if \mathcal{R} is positive (this shall not always be the case in this paper).

In numerical simulations, MOTSs are found on Cauchy surfaces in the course of a time evolution. Thus, if \mathcal{S} lies on a spacelike Cauchy surface Σ , and if R^a is the unit outgoing spacelike vector normal to \mathcal{S} , then it is natural to look at variations along R^a . This leads to the stability operator associated with Σ :

$$L_{\Sigma}[\psi] := \sqrt{2} \delta_{\psi R} \Theta_{(\ell)}, \quad (10)$$

where we used the freedom to choose a factor of $\sqrt{2}$ to simplify the following expressions. We label this stability operator by Σ instead of $L^{(\sqrt{2}R)}$ to emphasize the connection with the Cauchy surface. Since $R^a = (\ell^a - n^a)/\sqrt{2}$, we have (setting $\omega_a = 0$)

$$L_{\Sigma}[\psi] = \delta_{\psi \ell^a - \psi n^a} \Theta_{(\ell)} = \left(-\Delta_{\mathcal{S}} + \frac{1}{2} \mathcal{R} - 2|\sigma|^2 \right) \psi. \quad (11)$$

Since L_{Σ} and $L^{(-n)}$ are elliptic operators on a compact manifold, they have a discrete spectrum. In general these spectra are complex (due to the first derivative term involving ω_a). However the eigenvalue with smallest real part can be shown to be real, and is known as the principal eigenvalue Λ_0 . The corresponding eigenfunction ϕ_0 can be chosen to be positive. We note that the eigenvalues do not depend on the scaling of the null normals. If the null-normals are rescaled according to $\ell \rightarrow f\ell$, $n \rightarrow f^{-1}n$, then $L^{(-n)}$ undergoes a similarity transformation: $L^{(-n)} \rightarrow fL^{(-n)}f^{-1}$. The eigenfunctions of $L^{(-n)}$ are scaled by f but its eigenvalues are unaffected.

We now summarize some results and their connection to properties of the various horizons that we have already encountered in paper I. First we need a definition.

Definition 1 (Strictly-Stably-Outermost). *A MOTS \mathcal{S} is said to be strictly-stably-outermost along a direction X^a normal to \mathcal{S} if there exists some $\psi \geq 0$ such that $\delta_{\psi X} \Theta_{(\ell)} \geq 0$, and $\delta_{\psi X} \Theta_{(\ell)}$ does not vanish everywhere.*

This turns out to be equivalent to the principal eigenvalue being positive definite: $\Lambda_0 > 0$. If $\Lambda_0 > 0$ then we can choose ψ to be the lowest eigenfunction, and the condition $\delta_{\psi X} \Theta_{(\ell)} > 0$ follows. The converse is shown in [47]. The principal eigenvalue itself depends on the direction of X^a : it is largest for $X^a = -n^a$, and decreases as X^a turns towards ℓ^a . Two results are important for our purposes:

- *Starting with a MOTS on Σ , it evolves smoothly in time as long as L_Σ is invertible, i.e. none of its eigenvalues vanish. As a special case, this holds if $\Lambda_0 > 0$ whence all other eigenvalues also have positive real parts.*

The signature is also restricted if $\Lambda_0 > 0$:

- *Let \mathcal{S} be a strictly-stably-outermost MOTS. The world tube, i.e. the dynamical horizon, generated by the time evolution of \mathcal{S} is spacelike if $|\sigma|^2$ is non-zero somewhere on \mathcal{S} .*

In our simulation, this scenario applies for the individual dynamical horizons and for the outer common horizon. All of these turn out to be strictly-stably-outermost and, as we saw in paper I, they are all spacelike. The inner horizon is, as in other aspects, much more interesting. It has $\Lambda_0 < 0$, and as we saw in paper I, its signature is not restricted to be spacelike. The spectra of L_Σ and $L^{(-n)}$ will be described in detail in Sec. III.

C. Invariant coordinates on an axisymmetric horizon

For physical applications to be studied below, it will be important to decompose various fields on the horizons which have topology $S^2 \times \mathbb{R}$. These fields will be scalar, vector and second rank tensors. For a given MOTS \mathcal{S} , some important geometric fields of interest are the intrinsic curvature scalar \mathcal{R} , the rotational 1-form ω_a and the shear. Thus, it is very important to have a canonical notion of scalar, vector and tensor spherical harmonics or equivalently, spin weighted spherical harmonics. Different choices of spherical coordinates (θ, ϕ) on a MOTS will in general yield different multipolar decompositions. On an axisymmetric horizon, it turns out to be possible to construct an invariant coordinate system following [50].

We exploit the manifest axisymmetry present in our calculations, i.e. the existence of an axial vector φ^a which preserves the 2-metric q_{ab} on the horizon. For an axisymmetric surface \mathcal{S} of spherical topology \mathcal{S} with area $A_\mathcal{S}$ and radius $R_\mathcal{S} = \sqrt{A_\mathcal{S}/4\pi}$, we construct a coordinate system (θ, ϕ) adapted to φ^a . We assume that φ^a vanishes at precisely 2 points (the poles), and has closed integral curves. The coordinate ϕ is the affine parameter along φ^a , taken to be in the range $[0, 2\pi)$; we still need to fix the points with $\phi = 0$, which we shall do shortly. Second, the analog

of $\cos \theta$ is a coordinate ζ defined as follows:

$$\mathcal{D}_a \zeta = \frac{4\pi}{A_\mathcal{S}} \tilde{\epsilon}_{ba} \varphi^b, \quad \oint_{\mathcal{S}} \zeta dA = 0. \quad (12)$$

It follows obviously that $\mathcal{D}^a \zeta$ is orthogonal to φ^a and its integral curves are the lines of longitude connecting the two poles. Fix any one of these curves, and set $\phi = 0$ on it; this specifies ϕ completely. It is then straightforward to show that the 2-metric on \mathcal{S} can be written as

$$ds_q^2 = R_\mathcal{S}^2 \left(\frac{d\zeta^2}{F} + F d\phi^2 \right), \quad (13)$$

where

$$F(\zeta) = \frac{4\pi \varphi_a \varphi^a}{A_\mathcal{S}}, \quad (14)$$

and it can be shown that $-1 < \zeta < 1$ so that we can set $\cos \theta = \zeta$.

We can now write the spin weighted spherical harmonics in terms of (θ, ϕ) . It is important to note that the orthogonality relationships between the spherical harmonics continue to hold with the natural volume element on \mathcal{S} : in the volume element for the metric in Eq. (13), the factors of F cancel out. Thus, the volume element is identical to that of a fictitious canonical round 2-sphere metric

$$q_{ab}^{(0)} = R_\mathcal{S}^2 (d\theta^2 + \sin^2 \theta d\phi^2). \quad (15)$$

Spherical harmonics, including the spin weighted spherical harmonics, can be constructed in the usual way, but now using this canonical metric. Finally, a natural choice for the null vector m is

$$m = \frac{R_\mathcal{S}}{\sqrt{2}} \left(\frac{d\zeta}{\sqrt{F}} + i\sqrt{F} d\phi \right). \quad (16)$$

Thus, we have a complete null tetrad where (ℓ, n) is given by Eq. (4) and m is given here.

Having constructed the preferred coordinates on a given MOTS, let us now look at its time evolution and let \mathcal{H} be the dynamical horizon. For most of our results, the invariant coordinates described above suffice: at each instant of time, we can locate the axisymmetric MOTS, construct the invariant coordinate system, calculate the relevant physical quantity in this coordinate system, and then consider it as a function of time. There is no need to explicitly consider the problem of identifying points at different instants of time. In future work, when we do not have axisymmetry, this issue will be especially important if we wish to have a canonical notion of time evolution on \mathcal{H} . Even in this paper, it will be useful to clarify what one means by time evolution on \mathcal{H} .

Let us label the MOTSs on \mathcal{H} by a parameter λ (which in our case can just be the time coordinate of the numerical evolution) and let us consider a vector field X^a tangent to \mathcal{H} . In principle it need not necessarily be orthogonal to the MOTSs. The role of X^a is to evolve geometric fields from one MOTS to the next. In order to

talk about “time evolution” of fields and multipole moments on a dynamical horizon, it is necessary to have a canonical choice of X^a . One obvious choice is to take X^a such that it preserves the foliation of \mathcal{H} by MOTSs, and is orthogonal to the MOTSs. We shall call this vector field V^a . For concreteness, take \mathcal{H} to be spacelike everywhere so that we have a unit spacelike normal \hat{r}^a to each MOTS. Then, orthogonality of V^a to the MOTSs implies

$$V^a = a\hat{r}^a \quad (17)$$

with a being a function on \mathcal{H} . V^a preserves the foliation if we can choose $V^a\partial_a\lambda = 1$, and this naturally restricts a . We also require V^a to preserve the axial symmetry φ^a : $\mathcal{L}_\varphi V^a = 0$.

There are many situations where the above choice of V^a as evolution vector is not appropriate, and we need to add a shift vector N^a tangent to \mathcal{S} :

$$X^a = a\hat{r}^a + N^a. \quad (18)$$

An obvious example is when we have spinning black holes, so that we might need to add an angular velocity term: $X^a = a\hat{r}^a + \Omega\varphi^a$. Even for non-spinning black holes, it might be natural to have a non-vanishing shift vector. A general construction for X^a satisfying certain natural conditions is given in [51] to determine the “lapse” and “shift” for X^a as we move from one MOTS to the next. Let us briefly summarize the construction, specializing only later to the case when each MOTS is axisymmetric. An important condition, it turns out, is to choose X^a such that it preserves divergence free vector fields. The MOTSs are changing in area and thus the volume 2-form $\tilde{\epsilon}_{ab}$ is varying in time. We can think of this variation as being composed of i) an overall, homogeneous change corresponding to the overall area change, and ii) inhomogeneous variations on smaller scales which average away to zero on each MOTS. It turns out that the right condition is to choose X^a such that

$$\mathcal{L}_X \left(\frac{\tilde{\epsilon}_{ab}}{A_S} \right) = 0. \quad (19)$$

Note that the quantity $\tilde{\epsilon}_{ab}/A_S$ integrates to unity and contains the local inhomogeneous fluctuations in the area element on \mathcal{S} . Since this construction uses only invariantly defined geometric structures on \mathcal{H} , the axial symmetry vector φ^a is preserved, i.e.

$$\mathcal{L}_X \varphi^a = 0. \quad (20)$$

From the previous two equations and Eq. (12), it follows that ζ is preserved as well: $\mathcal{L}_X \zeta = 0$. Thus we construct the preferred coordinates (θ, ϕ) as above on each MOTS and then we simply take X^a such that ζ (or equivalently θ) remains fixed. We would still have the freedom to add a shift in the φ direction, but for non-spinning black holes, we can choose the shift to be completely in the ζ direction. In our case, it turns out that this construction leads to a non-zero shift vector in the ζ direction.

D. Fluxes, balance laws and multipole moments

We conclude this section by summarizing the flux law for spacelike dynamical horizons and the notion of multipole moments. The reason the area of a horizon increases is, of course, due to in-falling radiation and matter. The same applies to angular momentum, mass and higher multipole moments. This can be seen as a “physical process” version of the first law of black hole thermodynamics. For spacelike dynamical horizons it is possible to derive exact expressions for these fluxes in full non-linear general relativity. Since \mathcal{H} is spacelike, it is equipped with a unit timelike normal $\hat{\tau}^a$, and each leaf of \mathcal{H} has a unit spacelike normal \hat{r}^a tangent to \mathcal{H} . Then, a choice of null normals defined by \mathcal{H} is

$$\hat{\ell}^a = \frac{1}{\sqrt{2}}(\hat{\tau}^a + \hat{r}^a), \quad \hat{n}^a = \frac{1}{\sqrt{2}}(\hat{\tau}^a - \hat{r}^a). \quad (21)$$

This is analogous to Eq. (4), but the two choices are different and related by a scaling. Let A_i and A_f be the initial and final areas respectively of a (not necessarily infinitesimal) portion $\Delta\mathcal{H}$ of a spacelike dynamical horizon and let $\Delta R = R_f - R_i$ be the change in the area radius. Then, in vacuum spacetimes,

$$\Delta R = \frac{1}{4\pi} \int_{\Delta\mathcal{H}} \left(\hat{\sigma}_{ab}\hat{\sigma}^{ab} + 2\hat{\xi}_a\hat{\xi}^a \right) N_R d^3V. \quad (22)$$

Here $\hat{\sigma}$ is the shear of the outgoing null normal $\hat{\ell}^a$, $\hat{\xi}^a = \hat{q}^{ab}\hat{r}^c\nabla_c\hat{\ell}^a$, and N_R is a suitable lapse function. The integrand in this expression is manifestly positive definite. The important point here is that we have identified the shear and the vector $\hat{\xi}^a$ as the relevant fields which carry energy across \mathcal{H} . We have already written the shear as a complex field σ of spin weight 2, and we can similarly write $\hat{\xi}^a$ as a complex field $\hat{\xi} = \hat{\xi}^a m_a$ of spin weight 1. The identification of σ as an important part of the energy flux is similar to the flux across null surfaces [52]; see also [16, 48, 53–55]. The presence of the additional spin weight 1 field $\hat{\xi}$ occurs because we are here dealing with non-null surfaces. It is also worth noting that $\hat{\xi}$ becomes numerically difficult to calculate as \mathcal{H} approaches equilibrium and becomes null ($\hat{\tau}^a$ and \hat{r}^a are ill-behaved in the limit). Below we shall study the decomposition of σ into modes of spin weight 2, and their time evolution. Note that we shall use ℓ^a defined in Eq. (4) and not Eq. (21) for computing the shear and ξ .

Also of importance for us in this paper will be the notion of multipole moments [50] for axisymmetric horizons, analogous to the well known Geroch-Hansen multipole moments at infinity [56, 57]. These were first defined for isolated horizons where it can be shown that the two-dimensional scalar curvature \mathcal{R} and the rotational 1-form ω_a characterize the geometry of an isolated horizon. Thus, by considering multipole moments of these fields, one can characterize the horizon geometry completely with a set of multipole moments (see also [58]

for an alternate set of moments). These multipole moments continue to be useful even in dynamical cases [51]. Specifically, since we are dealing with non-spinning black holes, we only need to consider \mathcal{R} , which lead to the mass multipole moments of an axisymmetric MOTS \mathcal{S} :

$$I_l = \frac{1}{4} \oint_{\mathcal{S}} \mathcal{R} Y_{l,0}(\zeta) d^2V. \quad (23)$$

Here ζ is the invariant coordinate defined in Eq. (12), and $Y_{l,0}$ is the corresponding spherical harmonic. It is clear that the lowest moment I_0 is just a topological invariant, and for spherical topology $I_0 = \sqrt{\pi}$. Furthermore, I_1 can be shown to vanish identically from the definition of the coordinate system (in effect these invariant coordinates automatically place us in the center of mass of the system). Non-trivial information is obtained from $l = 2$ onwards, i.e. from the mass quadrupole, octupole etc.

III. THE SPECTRUM OF THE STABILITY OPERATOR

In this section we describe the spectrum of the stability operator for the various horizons. We consider mostly L_{Σ} , and $L^{(-n)}$ briefly (both have qualitatively similar features). We will break up the discussion into three parts considering in turn the principal eigenvalue, a selection of the next eigenvalues, and then finally a statistical analysis of the higher eigenvalues.

A. The principal eigenvalues

Beginning with the principal eigenvalues of L_{Σ} , we have already mentioned that for \mathcal{S}_1 , \mathcal{S}_2 , and $\mathcal{S}_{\text{outer}}$, Λ_0 is always positive. $\mathcal{S}_{\text{outer}}$ is born with $\Lambda_0 = 0$, but it immediately becomes positive and remains so. At early times for \mathcal{S}_1 and \mathcal{S}_2 , and at late times for $\mathcal{S}_{\text{outer}}$, two things happen: i) the flux $|\sigma|^2$ is small and thus the differences between L_{Σ} and $L^{(-n)}$ are small. ii) The scalar curvature \mathcal{R} has only small variations, and thus the spectrum of $L^{(-n)}$ is almost the same as that of the Laplacian on a round sphere, with a shift corresponding to the value of the curvature. Thus, in this limit where $\mathcal{R} \approx 2/R^2 = 1/2M_{\text{irr}}^2$ with R being the area radius, and M_{irr} being the irreducible mass, the eigenvalues are labeled by two quantum numbers (l, m) and will be approximately¹

$$\Lambda_{l,m} \approx \frac{1}{4M_{\text{irr}}^2} (1 + l(l+1)). \quad (24)$$

The state l is $(2l+1)$ -fold degenerate in this limit. In the general but still axisymmetric case, the degeneracy

between states of different $|m|$ is broken, with m being the label for the angular modes. The fundamental angular mode $m = 0$ will in general not be degenerate, while we find a 2-fold degeneracy ($\pm m$) for the higher modes with $m \neq 0$ due to axisymmetry. The principal eigenvalues of L_{Σ} are shown in Fig. 1 for all the horizons, whereas Fig. 2 shows the principal eigenvalues of $L^{(-n)}$. The main difference with L_{Σ} is that $\mathcal{S}_{\text{inner}}$ has positive principal eigenvalue for a short duration.

Most of this analysis does not apply to $\mathcal{S}_{\text{inner}}$. Just like $\mathcal{S}_{\text{outer}}$, the inner horizon $\mathcal{S}_{\text{inner}}$ is born with $\Lambda_0 = 0$. However unlike $\mathcal{S}_{\text{outer}}$, it becomes *negative* thereafter. $\mathcal{S}_{\text{inner}}$ is therefore unstable – it is not strictly stably outermost and there are thus no outward deformations which could make it strictly untrapped. It is also far too distorted for Eq. (24) to be even a rough approximation to its spectrum. We see from the right panel of Fig. 1 that Λ_0 for the inner horizon apparently diverges to $-\infty$ at T_{touch} where it has a cusp (though of course we cannot really prove this numerically).

This divergence, if it indeed exists, can be understood as follows. Given the structure of the stability operator, it is tempting to interpret it as the Hamiltonian of a quantum particle living on a sphere. The Laplacian is the analog of the kinetic energy while the other terms in $L^{(-n)}$ and L_{Σ} can be viewed as a potential. The ground state energy is then the analog of Λ_0 . This analogy can be extended also for spinning black holes where ω_a is non-vanishing [18, 19]. Then, the ground state energy will diverge to $-\infty$ only if the potential also diverges to $-\infty$. Of course, just because the potential diverges at a point does not mean the ground state energy also diverges; the hydrogen atom being the classic example. Whether or not $\Lambda_0 \rightarrow -\infty$ depends on the details of how \mathcal{R} diverges at the cusp². For $L^{(-n)}$, the potential is just $\mathcal{R}/2$, which is partially negative for $\mathcal{S}_{\text{inner}}$ near the cusp [1], and it diverges at T_{touch} . For L_{Σ} , the potential also contains $|\sigma|^2$ which complicates matters somewhat. However, since $|\sigma|^2$ is non-negative and comes with a negative sign, we see that the potential will still diverge. A detailed investigation of this mathematical question will take us too far afield from the goals of our numerical study here, and thus we will postpone this to future work.

There is one result for $\mathcal{H}_{\text{outer}}$ that will be important for us later, namely its approach to equilibrium. Having computed Λ_0 for $\mathcal{H}_{\text{outer}}$ at all times, we can ask how it approaches the equilibrium result of Eq. (24). For $l = 0$, we must have $\Lambda_0 \rightarrow \frac{1}{4M_{\text{irr}}^2}$ at late times whence we can compare $4M_{\text{irr}}^2\Lambda_0$ with unity. This is shown in Fig. 3 on a logarithmic scale. We see clearly a steep initial decay just after $T_{\text{bifurcate}}$, followed by a shallower decay and oscillations. We observe a transition between the two regimes

¹ Note that, for $l = 0$, this expression can be justified without assuming spherical symmetry (cf. Appendix B).

² This can be studied using the Lieb-Thirring inequality which relates the negative eigenvalues to the negative part of the potential (see e.g. [59]). In quantum mechanics, this inequality plays a critical role in mathematically proving that matter is stable.

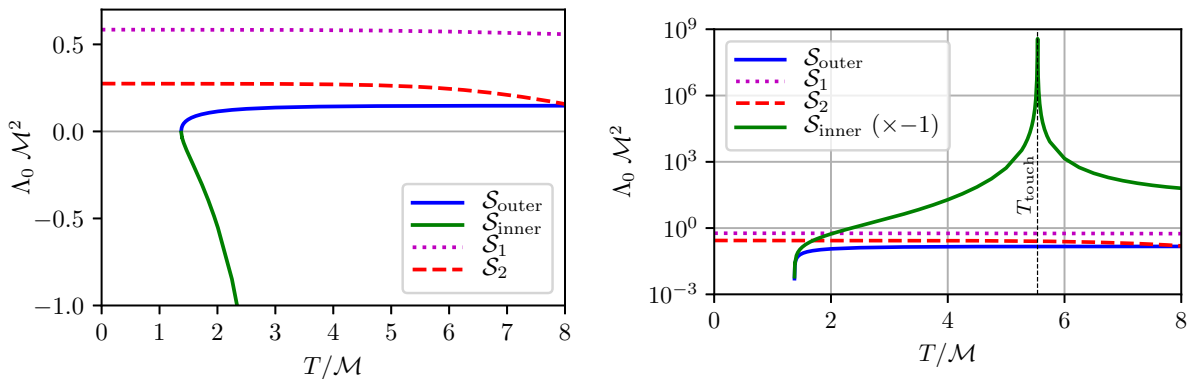


FIG. 1: The principal eigenvalue Λ_0 of L_Σ for all the horizons. Except $\mathcal{S}_{\text{inner}}$, all the horizons have positive Λ_0 . This is easily seen in the left panel. For $\mathcal{S}_{\text{inner}}$, Λ_0 shows a cusp at T_{touch} . This is shown in the right panel on a logarithmic scale (we plot $-\Lambda_0$ for $\mathcal{S}_{\text{inner}}$ because of the logarithmic scale).

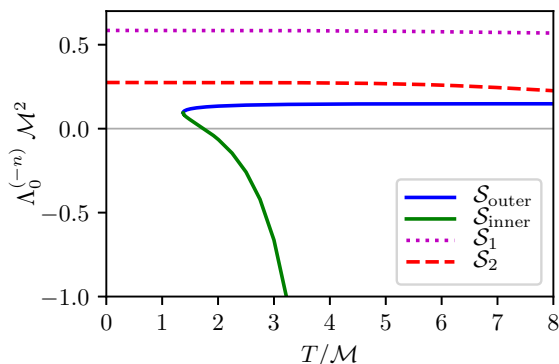


FIG. 2: The principal eigenvalue for $L^{(-n)}$ for the various horizons. These values turn out to be somewhat larger than the corresponding values for L_Σ . Thus, the bifurcation between $\mathcal{S}_{\text{inner}}$ and $\mathcal{S}_{\text{outer}}$ occurs at a positive value of Λ_0 . Thus, $\mathcal{S}_{\text{inner}}$ has positive principal eigenvalue for a short duration, and it does not cease to exist when Λ_0 crosses zero.

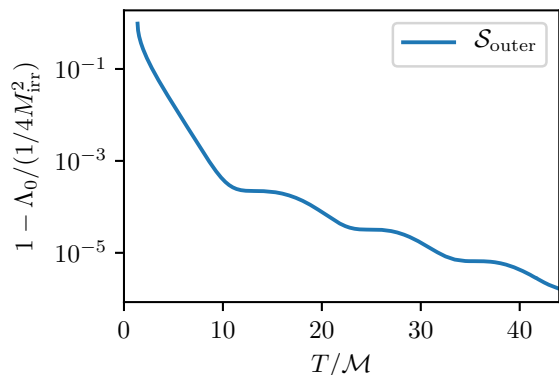


FIG. 3: Comparison of Λ_0 with the perturbative result (B4). Around $T \sim 10M$, the curve changes from a steep to a more shallow exponential decay.

at $\approx 10M$. This is our first encounter with this kind of behavior, and we shall see this same pattern repeatedly numerous times in this paper. We shall study this behavior quantitatively in detail for other geometric fields on $\mathcal{H}_{\text{outer}}$ in the following sections.

B. Low eigenvalues

For \mathcal{S}_1 , \mathcal{S}_2 and $\mathcal{S}_{\text{outer}}$, all the higher eigenvalues must be positive since $\Lambda_0 > 0$. Also for $\mathcal{S}_{\text{inner}}$, apart from Λ_0 , all other eigenvalues must be positive till T_{touch} . The reason is that at $T_{\text{bifurcate}}$, $\Lambda_0 = 0$ and all the other eigenvalues are positive definite. Since the evolution is smooth, the other eigenvalues must remain positive as long as $\mathcal{S}_{\text{inner}}$ exists. If any of these eigenvalues were to cross zero, $\mathcal{S}_{\text{inner}}$ would cease to exist. Fig. 4 therefore shows the next eigenvalue Λ_1 . It turns out to be positive with possibly a cusp at T_{touch} . This is shown in the second panel of Fig. 4. We see that the graph of Λ_1 as a function of time appears to be forming a cusp at T_{touch} , though we are not numerically able to resolve this. The precise value of Λ_1 at the cusp is of interest. If this were to be negative, then it means that Λ_1 vanishes before T_{touch} and therefore $\mathcal{S}_{\text{inner}}$ does not exist near the cusp. This seems unlikely since we find $\mathcal{S}_{\text{inner}}$ very shortly after T_{touch} . It seems more reasonable to assume that $\mathcal{S}_{\text{inner}}$ exists at all times around T_{touch} and our numerical methods are not able to locate it. This implies that the value of Λ_1 at T_{touch} should be non-negative. It would be interesting to prove (or disprove) this conjecture. In any event, Λ_1 is still far from vanishing at the last time before T_{touch} when it is located, indicating that it must exist for at least a short time longer. Similarly, at the first time it is located after T_{touch} , Λ_1 is similarly positive indicating that it must have existed for at least a short time earlier. Interestingly, the two lowest degenerate eigenvalues with angular modes $m = \pm 1$ are positive before T_{touch} , while after T_{touch} the lowest $m = \pm 1$ eigenvalues become nega-

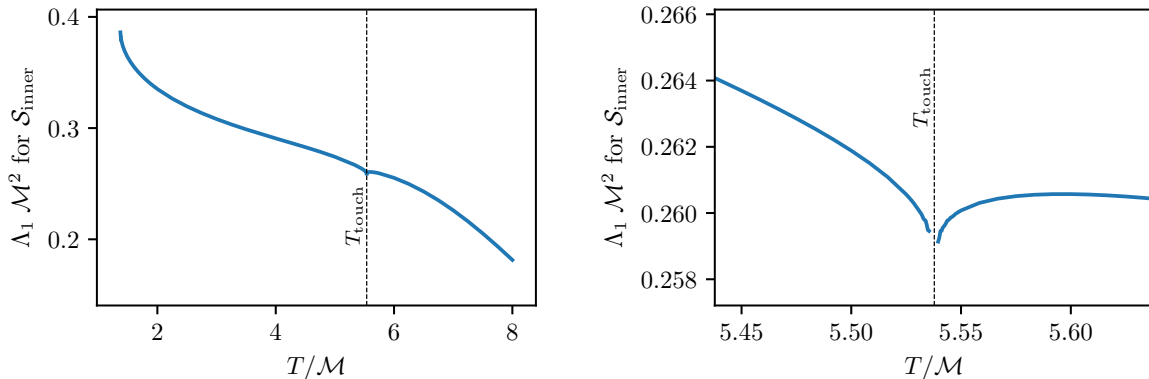


FIG. 4: The second eigenvalue Λ_1 for $\mathcal{S}_{\text{inner}}$ with angular mode $m = 0$. The second panel shows a close-up near T_{touch} . The graph appears to show cusp-like behavior at T_{touch} .

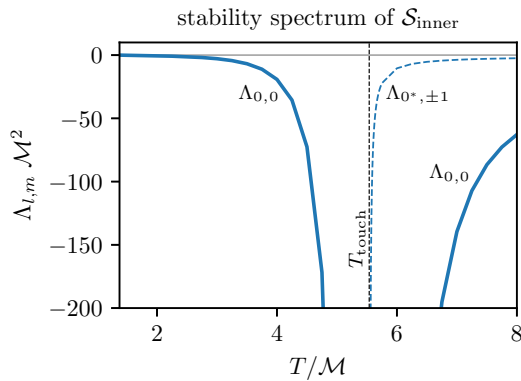


FIG. 5: The negative eigenvalues for $\mathcal{S}_{\text{inner}}$. After T_{touch} , two new (degenerate) negative eigenvalues appear for the $m = \pm 1$ angular modes.

tive. We chose to label these as new eigenvalues without relabeling the higher $m = \pm 1$ ones. That is, instead of the usual $\Lambda_{1,1} < 0 < \Lambda_{2,1} < \dots$ we assign the labels $\Lambda_{0^*, \pm 1} < 0 < \Lambda_{1,1} < \dots$. This is shown in Fig. 5. These $\Lambda_{0^*, \pm 1}$ eigenvalues are seen to increase much more rapidly than Λ_0 itself but, as far as we are able to track $\mathcal{S}_{\text{inner}}$, none of these eigenvalues cross zero and $\mathcal{S}_{\text{inner}}$ continues to exist.

C. Global behavior of the spectrum

The higher eigenvalues of L_Σ are shown³ in Fig. 6. The top panels show the spectra for \mathcal{S}_1 and \mathcal{S}_2 . At early times we have the behavior predicted by Eq. (24). The larger black hole, i.e. \mathcal{S}_2 , has smaller eigenvalues for the same

value of l . A multiplet structure is apparent here. As we get closer to the merger, the states with different m are no longer degenerate, analogous to the splitting of energy levels of a quantum system in an external field. The states with $\pm m$ remain degenerate due to axisymmetry. For generic configurations (including spins, non-zero orbital angular momentum etc.), this symmetry would then not be present and the $\pm m$ states would not be degenerate.

As we approach T_{touch} , the energy levels are seen to cross and it becomes more difficult to distinguish the states with different l , though the multiplet structure with splitting can still be identified. The apparent horizon has the opposite behavior. It approaches this simple spectrum at late times when it settles down to a Schwarzschild black hole. The multiplet structure here is again apparent.

The inner horizon $\mathcal{S}_{\text{inner}}$ apparently shows no such simplicity. Nevertheless, some spectroscopy-like analysis seems possible. In particular, a transfer of states between different multiplets seems to happen, with a migration of states from $l \rightarrow l + 2$. This can be understood in terms of tidal coupling. Specifically, at around $T \sim 3M$, $\mathcal{S}_{\text{inner}}$ is sufficiently deformed. It structures itself into two well identified lobes that ultimately pinch at T_{touch} . The system starts to effectively behave as a binary, dramatically illustrated by the eigenfunctions which situate themselves in either one or the other lobe (illustrated in Fig. 7). The two components of this “quasi-binary” interact tidally ($l = 2$) inducing this coupling in the spectrum levels.

In summary, this kind of non-trivial coupling between levels results in a completely different multiplet restructuring after T_{touch} (e.g. the two lowest multiplets are singlets, as a consequence of the loss of states to higher levels). Globally, there turns out to be a further complexity for the inner horizon that suggests the need to resort to other systematic tools to probe its underlying structure. Looking further ahead to future work when we consider more generic configurations without axisymmetry, the spectrum will be complex and yet more complicated.

³ The spectrum of $L^{(-n)}$ has similar global properties, except that we obtain slightly larger values corresponding to $|\sigma|^2$, and in accordance with the general results in [47]. We have chosen to show just the principal eigenvalue, cf. Fig. 2.

It will not be possible to investigate each eigenvalue in detail. We must then resort to a statistical analysis of the spectrum, from which we can extract valuable information. The remainder of this section can be seen as a precursor to the more complicated case.

1. Crossing of energy levels

Still in a spectroscopic spirit, a clearly evident feature of the spectra shown in Fig. 6, including that of $\mathcal{S}_{\text{inner}}$, is the crossing of eigenvalue levels. This is very significant, since it is not the generic situation for real self-adjoint operators (of the class we are studying) depending on a single parameter, time t in our case. The variation of the Hamiltonian with time typically leads to level repulsion, whereas level-crossing requires two parameters [60]. This can be accounted for in terms of the corresponding classical dynamics, if the operator is understood as a classical Hamiltonian on a phase space. It turns out that for generic classical Hamiltonian systems, namely non-integrable (or chaotic in rough terms), level-crossing translates into an over-determined condition which generically admits no solution if only one parameter is available. As a result, eigenvalues repel, something that quantum-mechanically corresponds to coupling of the levels and the impossibility of defining quantum numbers.

On the contrary, when the underlying classical motion is integrable, the eigenvalue curves indeed can (quasi-)cross⁴. Levels do not interact and evolve independently, quantum numbers can be tracked and clustering can happen due to the absence of level repulsion. In our present case, the corresponding classical system is not only integrable, but our problem is actually separable⁵ as a consequence of axisymmetry. The latter is a stronger (non-generic) feature that implies integrability [60]. From this perspective, nothing distinguishes $\mathcal{S}_{\text{inner}}$ from the other horizons. In summary, for the four spectra shown in Fig. 6, level-crossing is a strong indication of classical integrability and in our case a confirmation of the a priori knowledge about the separability of the system.

⁴ Actual crossing requires a stronger condition, namely separability, whereas in general integrable systems level lines can approach to extremely narrow separations but can then ultimately repel [60].

⁵ An interesting consequence of the separability of our eigenvalue problem, as a consequence of axisymmetry, is the crossing of nodal lines of the eigenfunctions. This is not the generic situation even for integrable system (c.f. e.g. [61]), and follows from separability in two-dimensions in an orthogonal coordinate system. This is illustrated in Fig. 7 for two eigenfunctions of $\mathcal{S}_{\text{inner}}$.

2. Spectrum statistics

The spectrum of a given MOTS stability operator is of course purely deterministic and can be efficiently calculated numerically. The underlying system, black holes in standard classical general relativity, do not have any quantum aspects. However, we have found it useful to think of the spectral problem as being associated with the Hamiltonian of a quantum particle living on the MOTS. We shall now push this analogy further to the higher eigenvalues and borrow techniques from quantum mechanics. In the present self-adjoint setting the operators $L^{(-n)}$ and L_{Σ} can be seen (cf. sec 4.4. in [18]) as the quantum Hamiltonian \hat{H} corresponding to a classical Hamiltonian function $H(p, q) = q^{ab}p_a p_b + \frac{1}{2}\mathcal{R}(q)$ on the cotangent bundle T^*S . Much insight can be gained then into the actual MOTS spectrum from semi-classical considerations connecting the quantum system defined by \hat{H} to the underlying classical Hamiltonian system [60, 62–65]. Tools and concepts from the study of quantum chaos will be adapted to the present MOTS setting. Different eigenvalue-level statistics can be devised to address distinct aspects of the spectrum. We will focus here on the small scale aspects of the spectrum, i.e. the interaction between adjacent levels.

For the higher eigenvalues, a statistical perspective on the distribution of eigenvalues can reveal important structural features of the underlying geometric object. This approach parallels the research program initiated by Wigner [66] to undertake the understanding of the spectral properties of complex heavy nuclei in terms of statistical ensembles, leading to Dyson’s random-matrix models [67–69]. Later, these tools have been also systematically employed in the setting of quantum chaos, exploring the subtle interplay between the quantum and the underlying semi-classical system. Here we will focus on the application to our spectra of a short-range correlation in the spectrum, namely the ‘nearest neighbor spacing distribution’ $P(S)$ which we describe shortly. This spectral statistic accounts for the fine-scale structure of the spectrum and in particular it is sensitive to the clustering or repulsion between the energy levels.

An important point is a need to remove “trivial” degeneracies due to symmetries. In our case these degeneracies correspond to the $\pm m$ degeneracy. We do not want the distribution $P(S)$ to be dominated by this degeneracy, and thus they must be removed at the very start of the analysis. Eigenvalues can then be ordered as

$$\Lambda_o < \Lambda_1 \leq \Lambda_2 \leq \dots \leq \Lambda_n \leq \dots, \quad (25)$$

where the non-degeneracy of Λ_o has been taken into account.

Prior to the introduction of spectral statistics, we perform a normalization of the spectrum by setting its average level density to unity. Specifically, we first introduce a function $N(\Lambda)$ counting the number of eigenvalues Λ_i

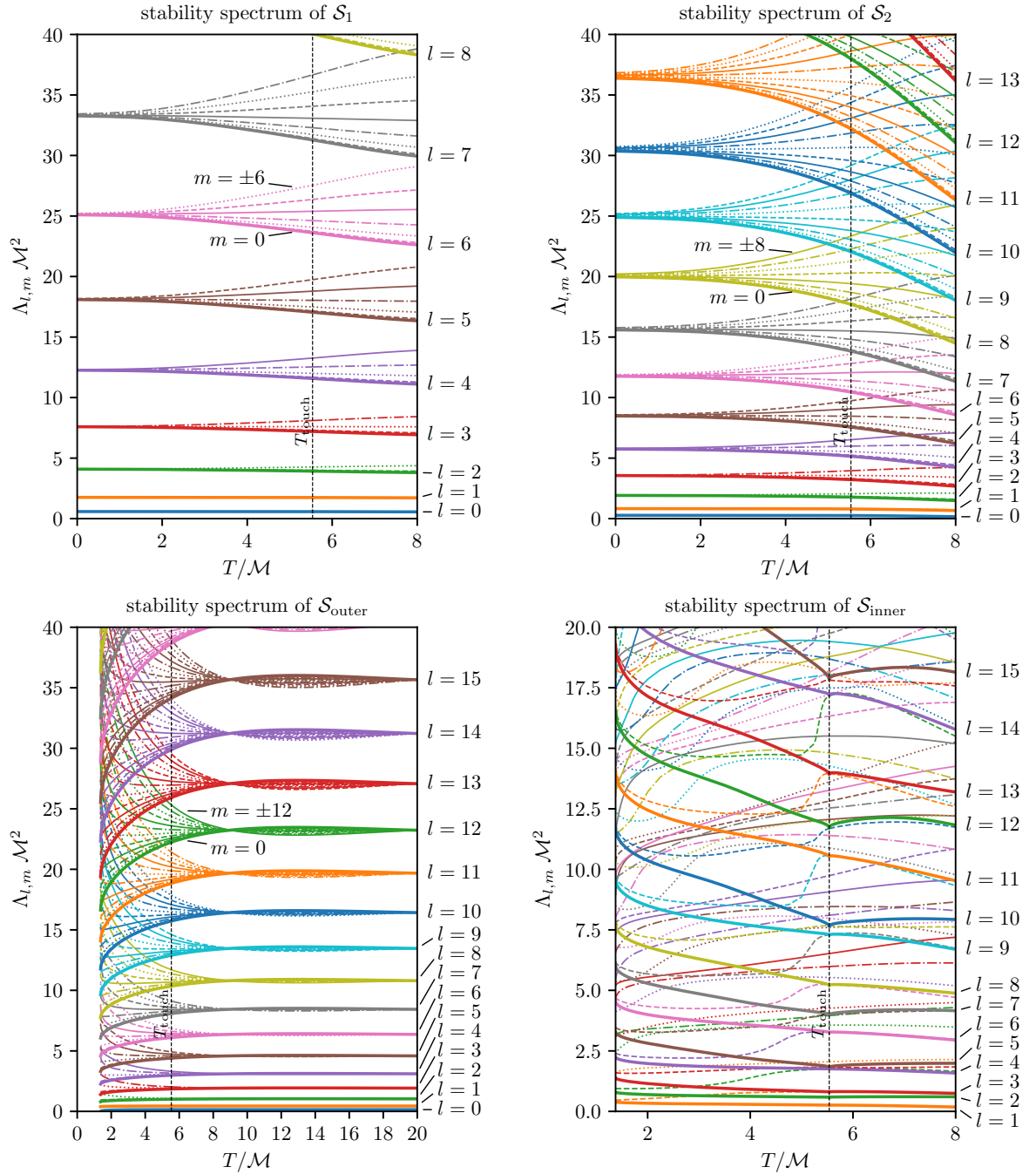


FIG. 6: The stability spectrum of the various horizons. As expected, \mathcal{S}_1 and \mathcal{S}_2 (top two panels) start off with a simple spectrum corresponding to Eq. (24) and become more complicated near the merger. The spectrum for $\mathcal{S}_{\text{outer}}$ in the bottom-left panel shows the opposite behavior. The bottom right panel shows the positive part of the spectrum for $\mathcal{S}_{\text{inner}}$.

below a certain value Λ as

$$N(\Lambda) = \sum_i \Theta(\Lambda - \Lambda_i), \quad (26)$$

where $\Theta(y) = 1 - H(y)$, with $H(y)$ the Heaviside function. The counting function $N(\Lambda)$ has a staircase structure. The level density (density of states) is then defined

as

$$\rho(\Lambda) = \frac{dN}{d\Lambda}. \quad (27)$$

We can write $N(\Lambda)$ as

$$N(\Lambda) = N_{\text{av}}(\Lambda) + N_{\text{fl}}(\Lambda). \quad (28)$$

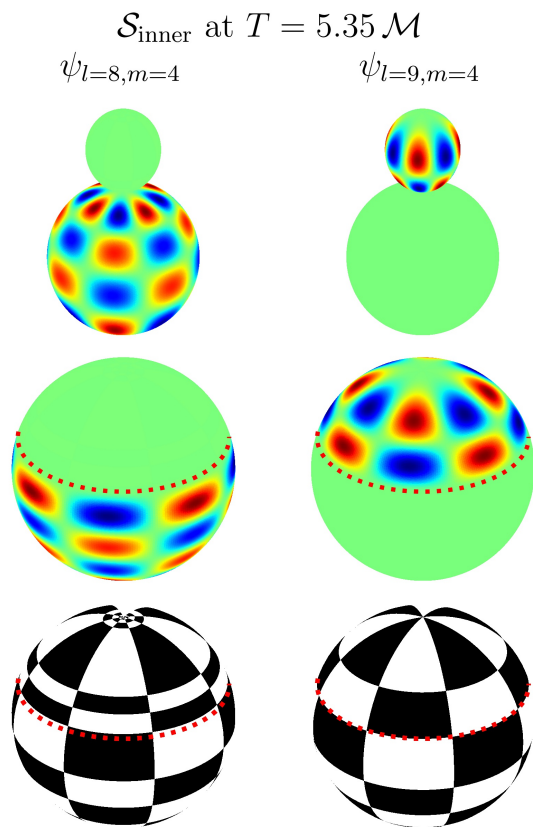


FIG. 7: Visualization of two eigenfunctions $\psi_{l,m}$ of L_Σ for $\mathcal{S}_{\text{inner}}$ at a time $T = 5.35 \mathcal{M}$ before $T_{\text{touch}} \approx 5.53781 \mathcal{M}$. The top row shows the function values in blue (< 0) and red (> 0) on $\mathcal{S}_{\text{inner}}$, while the lower two rows show the function values and sign changes, respectively, as functions of (θ, ϕ) on a sphere.

The dotted line indicates the θ -coordinate of the “waist” visible in the first row. From the bottom row it is clear that the extended green regions are only close to zero but still contain structure.

Here $N_{\text{av}}(\Lambda)$ is a monotonically increasing smooth function; it is the secular part of $N(\Lambda)$ interpolating the steps in $N(\Lambda)$. $N_{\text{fl}}(\Lambda)$ is the fluctuating part accounting for the difference with respect to the secular increase. The “unfolding” of the spectrum is a “rectification” of the latter such that secular level density is 1. In particular, by introducing $x = N_{\text{av}}(\Lambda)$, for the “unfolded spectrum”

$$x_i = N_{\text{av}}(\Lambda_i), \quad (29)$$

we obtain an average level density of unity in the new variable

$$\rho_{\text{av}}(x) = \frac{dN_{\text{av}}}{dx} = \frac{dN_{\text{av}}}{d\Lambda} \frac{d\Lambda}{dx} = \frac{dN_{\text{av}}}{d\Lambda} \left(\frac{dN_{\text{av}}}{d\Lambda} \right)^{-1} = 1. \quad (30)$$

We focus here on the fine scale features in the spectrum, in terms of the distribution of separations between adjacent eigenvalues in Eq. (25). Nearest-neighbor spacings

S_i are calculated in the unfolded spectrum as

$$S_i = x_{i+1} - x_i. \quad (31)$$

The probability of finding a spacing between S and $S+dS$ is given by $P(S)dS$ and, because of using the unfolded spectrum, the average spacing $\langle S \rangle$ is unity:

$$\langle S \rangle = \int P(S)SdS = 1. \quad (32)$$

Since $P(S)$ measures the correlation between adjacent eigenvalues, $P(S)$ is said to be a “short-range level” correlation measure. We shall calculate $P(S)$ for the stability spectrum and attempt to interpret the result as a representative of a particular universality class. As a trivial example of such a universality class, consider the so-called “picket fence” distribution (namely a Dirac delta) centered at unity:

$$P(S) = \delta(S - 1). \quad (33)$$

It is clear that such a distribution characterizes a perfectly regular spectrum.

More interestingly, for real Laplacian-like operators as in Eqs. (9) and (11), $P(S)$ presents a universality behavior according to the type of classical motion, ‘integrable’ versus ‘chaotic’, of the corresponding classical Hamiltonian:

- i) “*Integrable*” classical motion: In this case we obtain a Poisson distribution

$$P(S) = e^{-S}. \quad (34)$$

This corresponds to a distribution showing a tendency to cluster since $P(0) \neq 0$. Moreover, the levels $\Lambda(t)$ cross⁶. In particular, crossing happens for separable systems. The associated degeneracy is accounted by a non-vanishing $P(0)$ and quantum numbers can be assigned to levels in a straightforward manner.

- ii) “*Chaotic*” classical motion: This is the so-called

⁶ They can actually repel at an exponentially small scale [60].

Wigner surmise ⁷:

$$P(S) = \frac{\pi}{2} S e^{-\frac{\pi S^2}{4}}. \quad (36)$$

This behavior displays repulsion between eigenvalues since $P(0) = 0$. The eigenvalue curves (generically) do not cross [60], and therefore they do not degenerate. Level crossing requires two parameters. Therefore close levels couple and repel, with the strength of the coupling given by the minimum energy difference between the two repelling eigenvalue curves. No “quantum numbers” can be assigned to such levels.

It is important to keep in mind that any of this behavior becomes evident only after the “trivial” degeneracies due to symmetries have been eliminated. Long-range correlations can be studied with other spectral statistics (cf. e.f. [65]), such as the number variance $\Sigma(L)$ or the spectral rigidity $\Delta(L)$, presenting also universality in certain regimes (small L in this case). We postpone this to a later study.

We are now ready to apply the above formalism to the stability spectrum. We start by mapping the spectrum to the “unfolded” spectrum where the average spacing between neighboring levels is normalized to 1. For this we first determine the average $N_{\text{av}}(\Lambda)$ of the spectrum level-counting function $N(\Lambda)$. Fig. 8 shows in panel (a) the step-wise $N(\Lambda)$ for all four horizons at a time very close to T_{touch} . In particular, we note the nice agreement with Weyl’s law (see Appendix A) at large eigenvalues.

Then defining the unfolded levels as $x_i = N_{\text{av}}(\Lambda_i)$, we can construct the distribution of the nearest-neighbor distance variable, $S_i = x_{i+1} - x_i$. First we notice that if only eigenvalues with a fixed m are considered, then we obtained a perfectly regular distribution corresponding to a “picket fence” centered at $S = 1$ given in Eq. (33). This case is shown in panel (c) of Fig. 8. This is non-generic behavior, resulting from axisymmetry where m is the only preserved quantum number for all times. The distribution is dominated by this degeneracy and we are

not able to infer any relevant non-trivial structure. To fix this, consider now all eigenvalues with the $\pm m$ symmetry removed. The resulting histogram for $P(S)$ is shown in Fig. 8, panels (b) and (e). As expected, a Poisson distribution is obtained for both $\mathcal{S}_{\text{outer}}$ and $\mathcal{S}_{\text{inner}}$ despite their very different appearance in Fig.6. This is a consequence of the underlying classical integrability. The effect of level-crossing is apparent in the non-vanishing value of $P(0)$, indicating the generic occurrence of degeneracies.

Finally, we comment on the oscillations of the eigenvalues visible in Fig. 6. For example, near $T \approx 9\mathcal{M}$, we see from the bottom-left panel of the figure that the eigenvalues with the same l (but different m) are apparently almost degenerate. Remarkably at this time, the spectrum is in fact very close to that of a round sphere – the various oscillation modes of the MOTS conspire near this time to produce a nearly round sphere for a short duration. Panel (f) of Fig. 8 shows the distribution $P(S)$ at this time. This is very close to a quasi-picket-fence distribution centered at $S = 0$ in. As we shall explain later, this behavior is consistent with the observed evolution of the horizon multipoles in Fig. 16.

Regarding $\mathcal{S}_{\text{inner}}$, we note that the $P(S)$ statistic does not capture many specific features of the spectrum. This includes, for example, the multiplet reorganization between different levels, which is not a short-correlation effect. Addressing this requires the implementation of statistics for long-range correlations among spectrum levels, such as the number variance $\Sigma(L)$ or the spectral rigidity $\Delta(L)$, and will be done somewhere else. Finally, the present spectrum statistics analysis could have been anticipated from the a priori knowledge of the system separability. The interest therefore lies in providing a benchmark for future comparison with generic binary mergers where separability will be lost and, presumably, classical integrability will also disappear.

IV. HORIZON SHEAR AND FLUXES

Paper I has provided a detailed understanding of how the area increases. Now we turn our attention to *why* the area increases, i.e. because of the in-falling flux of radiation (and potentially matter fluxes if we had matter fields). Recall here the expression for the area flux given in Eq. (22). There are two contributions, the first being the familiar shear term. This is analogous to the well known outgoing radiation at least in the sense that the shear is a field of spin weight 2. It has been observed to be closely correlated with the News tensor at null infinity [16]. The second term involving ξ has no corresponding counterpart at null infinity (this is not surprising given that the dynamical horizon is not null). Being a vector field, $\xi = \xi_a m^a$ has spin weight +1.

The dominant term in the flux is the shear. Let us therefore consider the 2-dimensional integral of $|\sigma|^2$ over the various MOTSs; let us call this the shear flux. The result is shown in Fig. 9. The shear-flux increases for \mathcal{S}_1

⁷ Very interestingly, the Wigner surmise appears also in the setting of the Gaussian Orthogonal Ensemble (GOE) universality class in random matrices. More generally, the Bohigas-Giannoni-Schmit conjecture (cf. e.g. [65]), the eigenvalues corresponding to a chaotic classical system obey the same universal statistics of level spacings as those Gaussian random matrices [67–69]. In particular, real time-reversal symmetric systems follow Gaussian Orthogonal Ensemble (GOE) statistics, whereas (complex) non-time-reversal symmetric Hamiltonians are associated with the Gaussian Unitary Ensemble (GUE). Other “more exotic” non-time-reversal systems, appearing for instance in spin systems, are related to the Gaussian Symplectic Ensemble (GSE). For completeness, we present here the universal $P(S)$ distributions for GUE and GSE statistics

$$P_{\text{GUE}}(S) = \frac{32}{\pi} S^2 e^{-\frac{\pi 4 S^2}{\pi}}, \quad P_{\text{GSE}}(S) = \frac{2^{18}}{3^6 \pi^3} S^3 e^{-\frac{64 S^2}{9\pi}}. \quad (35)$$

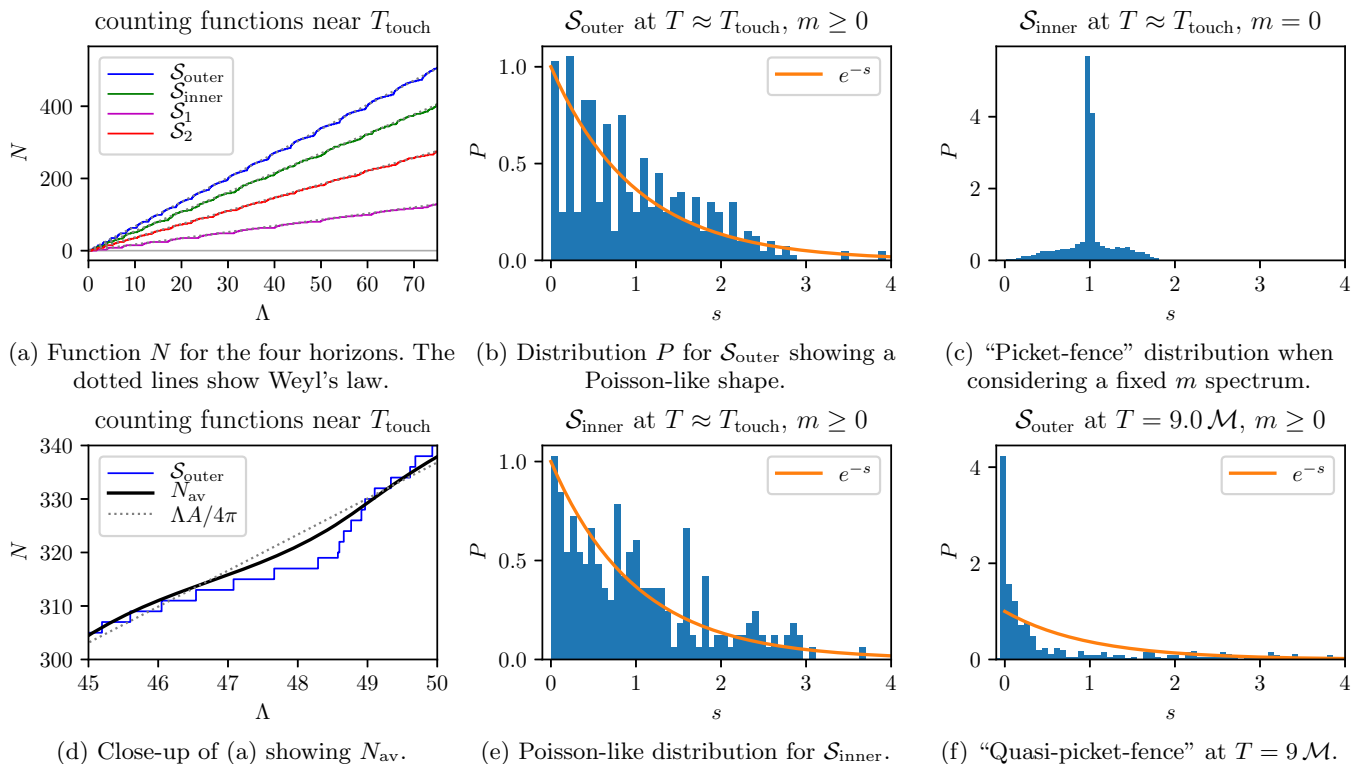


FIG. 8: Construction and examples of the spectrum statistics. See text for details.

and \mathcal{S}_2 , while it decreases for $\mathcal{S}_{\text{outer}}$. The dip in the shear-flux for $\mathcal{S}_{\text{outer}}$ near $T \approx 13\mathcal{M}$ is because of an oscillation in the dominant $l = 2$ mode of the shear as we shall see below. This is to be compared with Fig. 10 of paper I showing the corresponding dip in the plot of the rate of change of the area as a function of time. For the inner-common horizon $\mathcal{S}_{\text{inner}}$, the shear-flux increases rapidly in the beginning and soon reaches a plateau. It is noteworthy that there is no discontinuity across the merger when $\mathcal{S}_{\text{inner}}$ develops a cusp and then self-intersections.

Being a symmetric tracefree tensor, we expand σ in spherical harmonics of spin weight $+2$. We have already constructed in Sec. II C a preferred coordinate system (θ, ϕ) which exploits the axisymmetry of the problem. These coordinates can obviously also be used for our needs in this section, i.e. expanding spin weight 2 fields. For the complex scalar σ we get

$$\sigma(\theta, \phi, t) = \sum_{l=2}^{\infty} \sum_{m=-l}^l \sigma_{lm}(t) {}_2Y_{lm}(\theta, \phi). \quad (37)$$

Here ${}_2Y_{lm}$ are spin-weighted spherical harmonics and σ_{lm} are the mode amplitudes. This decomposition can be carried out for all of the horizons in our problem, namely the two individual and the two common horizons. Furthermore, since we have explicit axisymmetry with σ independent of ϕ , we will only have the $m = 0$ modes and we will drop the index m in $\sigma_{l,m}$.

Fig. 10 shows $|\sigma_l|$ for the two individual horizons, for $l = 2, 3, \dots, 12$. As the figure shows, the mode amplitudes

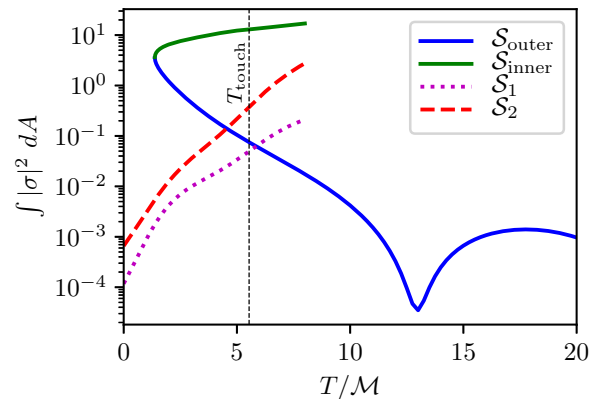


FIG. 9: The integral of $|\sigma|^2 := \sigma_{ab}\sigma^{ab}$ for the outgoing normal ℓ^a given in Eq. (4). The dashed and dotted lines are for the individual horizons while the solid lines are for the two common horizons.

decrease monotonically as the mode index l increases, so that the $l = 2$ mode dominates. Similarly, as expected, the shear generally increases with time, indicating larger fluxes as we approach the merger. This is confirmed by the integrals of $|\sigma|^2$ over \mathcal{S}_1 and \mathcal{S}_2 shown in Fig. 9.

Fig. 11 shows the shear modes for the inner and outer horizons. These have a number of interesting features worth pointing out. Consider first the shear on the apparent horizon which is expected to be correlated with

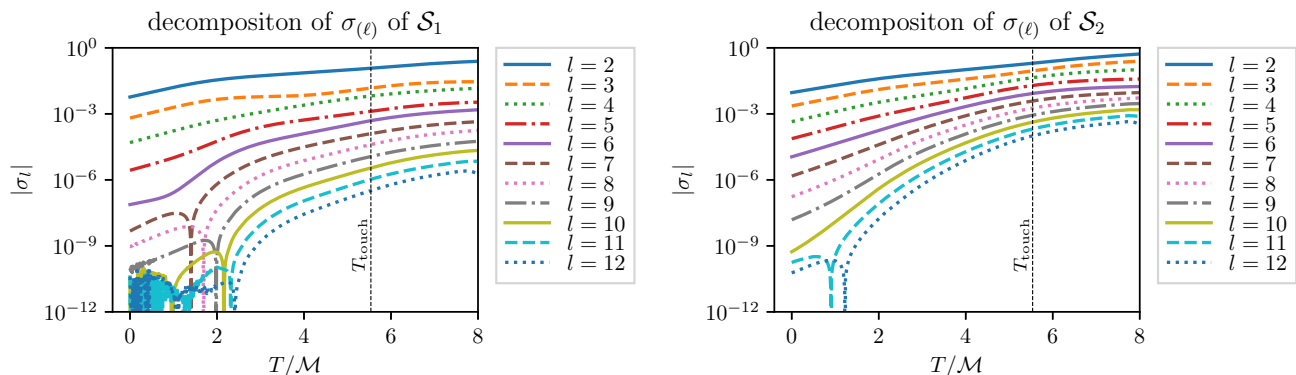


FIG. 10: The mode decomposition of the shear for the two individual black holes. See text for details.

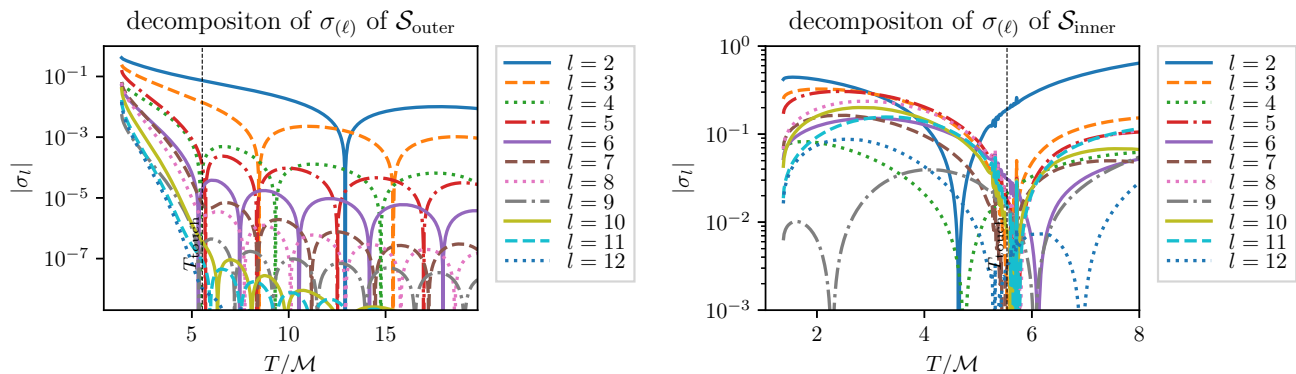


FIG. 11: Shear modes for the common horizons. The left panel shows $|\sigma_l|$ for the outer common horizon and the right panel shows the mode coefficients for the inner horizon. See text for further discussion.

the post-merger gravitational waveform measured in the wavezone far away from the source. It was observed in [15] that the horizon multipole moments (which will be discussed below) fall-off exponentially with decay rates consistent with the quasi-normal mode frequencies of the final black hole. Moreover, it was shown that the fall-off of the multipole moments is well explained by the presence of two exponentially damped modes. This is consistent with [70] which observed that the post-merger waveform is well explained by the quasi-normal modes, including the higher overtones. Motivated by these results, we consider a model for the shear amplitude $|\sigma_l(t)|$ with two exponentially damped modes:

$$\sigma_l(t) = A_l^{(1)} e^{\alpha_l^{(1)} t} + A_l^{(2)} e^{-i\alpha_l^{(2)} t}. \quad (38)$$

Here we take $\alpha_l^{(1)}$ to be real, and $\alpha_l^{(2)}$ to be complex because, as shown below, at early times the shear does not show any oscillations, while at later times it exhibits damped oscillations. When one mode falls off much more rapidly than the other, a simplified piecewise-exponential model can be used:

$$\sigma_l(t) = A_l^{(1)} e^{\alpha_l^{(1)} t}, \quad 0 < t < t^{(1)}, \quad (39)$$

$$\sigma_l(t) = A_l^{(2)} e^{-i\alpha_l^{(2)} t}, \quad t > t^{(2)}. \quad (40)$$

Again, the early part is just exponentially damped, while the later part is an exponentially damped oscillation. We do not necessarily choose $t^{(1)} = t^{(2)}$. In practice, we find that one of the modes is rapidly decaying with an initially larger amplitude, and a second mode which is longer lived but with lower initial amplitude. This simplified model with suitably chosen transition times $t^{(1,2)}$ will therefore suffice for our purposes. Before presenting the best fit values of the decay rates, it is instructive to look at some of the fits to the individual modes in Fig. 12. For this figure and the following fitting results, our simulation with the lower resolution of $1/\Delta x = 60$ and $T_{\max} = 50M$ was used in order to obtain late time data for the outer horizon $\mathcal{H}_{\text{outer}}$. It is clear from these plots that the mode amplitudes have qualitatively different fall-offs at early and late times with the transition occurring roughly between $T = 8M$ and $T = 10M$. It is also clear that accurate values of $\alpha_l^{(1)}, \alpha_l^{(2)}$ respectively will be obtained by taking $t^{(1)}$ as small as possible, and $t^{(2)}$ as large as possible; we take $t^{(1)} = 4$ and $t^{(2)} = 20$. Finally, the fits of the imaginary part $\Im(\alpha_l^{(2)})$ are obtained by considering the local maxima of $|\sigma_l|$ after $t^{(2)}$, and the real part $\Re(\alpha_l^{(2)})$ is obtained by looking at the zero-crossings of σ_l .

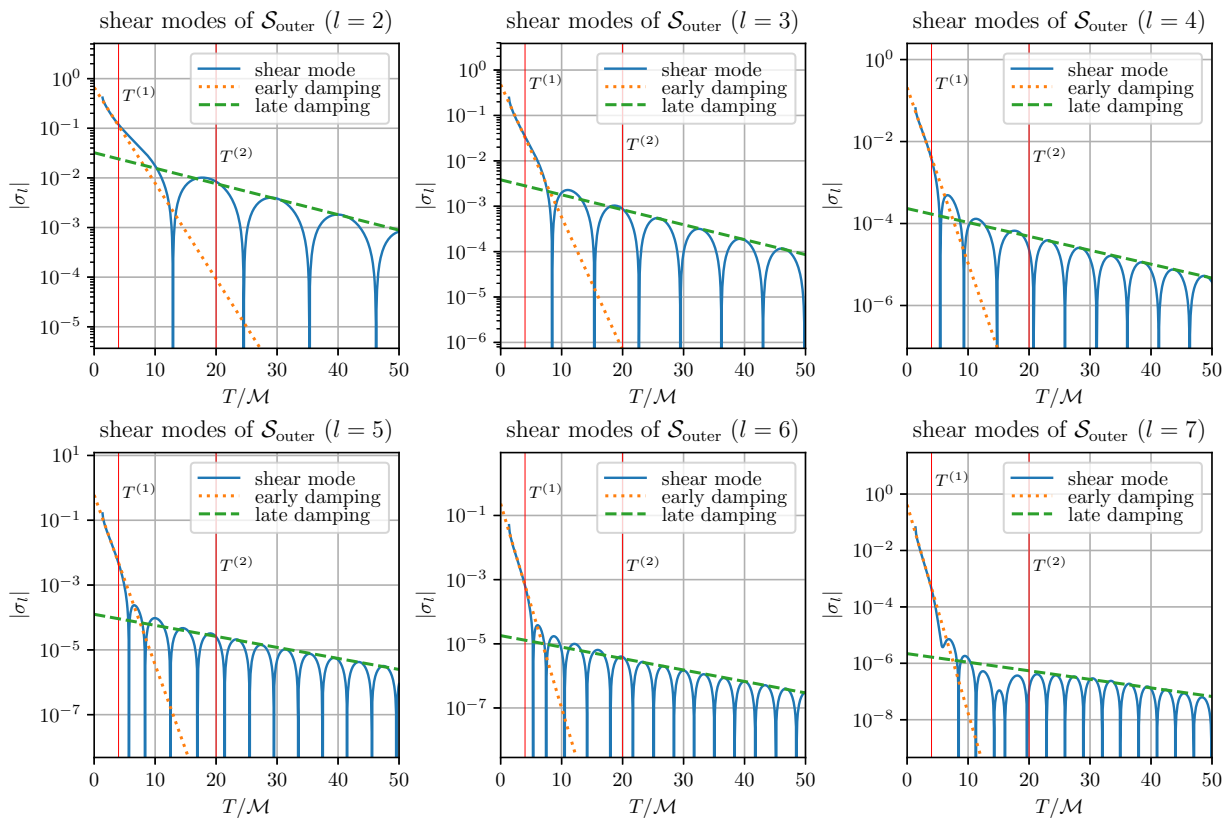


FIG. 12: Fits of the shear mode for $l = 2, 3, \dots, 7$. The curves in blue show the shear amplitude, the orange dotted line shows the exponential fit at early times (before $T^{(1)} = 4\mathcal{M}$), and the dashed green line is the exponential fit at late times (after $T^{(2)} = 20\mathcal{M}$). In each case we see a clear transition from steep decay to a slower decay rate.

Before looking at the best fit values obtained for the parameters in the above model, it will be useful to keep in mind the values of the standard quasi-normal mode frequencies for a Schwarzschild black hole. Quasi-normal modes are defined in the framework of perturbation theory, and they are solutions which are purely outgoing at the horizon and at infinity [71, 72]. This condition leads to a discrete set of complex frequencies labeled just by the mass of the black hole (for spinning and charged black holes, these would be determined by the mass, spin and charge). The complex frequencies are labeled by three integers (n, l, m) : (l, m) are the usual angular quantum numbers while $n = 1, 2, \dots$ is the overtone index for the radial wave-function. For a Schwarzschild black hole we only need to consider $m = 0$. Some values of the imaginary part of the frequency are shown in Table I. Similarly, it will be useful to know the real part of the frequency of the lowest ($n = 1$) overtone for different values of l . For $l = 2, 3, \dots, 7$ these are given in Table II. Detailed data files are available at [73], based on [74, 75]. It is useful to note that the imaginary frequency for a given overtone index n is fairly insensitive to the value of l , but for a given l , the higher overtones are damped more rapidly.

At late times, we fit separately for the oscillatory and

TABLE I: Some values of the imaginary Schwarzschild quasi-normal-mode frequencies for different (n, l) (taken from [73]).

	$n = 1$	$n = 2$	$n = 3$	$n = 4$
$l = 2$	-0.0890	-0.2739	-0.4783	-0.7051
$l = 3$	-0.0927	-0.2813	-0.4791	-0.6903
$l = 4$	-0.0942	-0.2843	-0.4799	-0.6839
$l = 5$	-0.0949	-0.2858	-0.4803	-0.6786
$l = 6$	-0.0953	-0.2866	-0.4806	-0.6786
$l = 7$	-0.0955	-0.2872	-0.4807	-0.6773

TABLE II: Some values of the lowest overtone ($n = 1$) of the real Schwarzschild QNM frequency for $l = 2, 3, \dots, 7$ taken from [73].

$l = 2$	$l = 3$	$l = 4$	$l = 5$	$l = 6$	$l = 7$
0.3737	0.5994	0.8092	1.0123	1.2120	1.4097

damped parts. We fit $\Im(\alpha_l^{(2)})$ by looking at the local maxima of $|\sigma_l|$ and fitting them to a straight line (on a logarithmic scale), while we fit $\Re(\alpha_l^{(2)})$ by looking at its zero crossings. The fits for the early part before $4\mathcal{M}$ turn out

to depend sensitively on the time $t^{(1)}$ in Eq. (39). The choice $t^{(1)} = 4$ was made to roughly minimize these variations. Similarly, to get accurate values we choose to use $t^{(2)} = 20$.

Let us now look at best fit values of the exponents. The best fit values for $\alpha^{(1)}$ and $\alpha^{(2)}$ are shown in Tab. III scaled with the ADM mass set to unity. Comparing the best fits for the real and imaginary parts of $\alpha^{(2)}$ with Table II and the first column of I, we find consistency over all the 6 modes considered. This leads us to believe that at late times the shear modes are associated with the fundamental overtone of the quasi-normal modes.

Things are not so clear with $\alpha^{(1)}$. Recent work has found that in binary black hole merger waveforms, the immediate post-merger signal is consistent with the higher overtones of the quasi-normal modes [70, 76–78]. It is thus tempting to think that $\alpha^{(1)}$ should be connected with the higher overtones. However, comparing the best fit values of $\alpha^{(1)}$ in Table III with the complex frequencies for the higher overtones given in Table I, we find no compelling evidence here. It is possible that a combination of these higher overtones could be considered, but we shall not attempt to do so here.

TABLE III: Fits of the shear modes based on the piecewise-exponential model of Eqs. (39) and (40). We show the coefficients $\alpha_i^{(1)}$ of early times ($T < 4M$) and $\alpha_i^{(2)}$ for late times ($T > 20M$). For $l < 7$, we estimate the errors of $\Re(\alpha_i^{(2)})$ to be about 1% and of $\Im(\alpha_i^{(2)})$ to be about 10%. All values have been scaled to correspond to a $M_{\text{ADM}} = 1$ simulation.

l	$\alpha_i^{(1)}$	$\Re(\alpha_i^{(2)})$	$\Im(\alpha_i^{(2)})$
2	-0.578	0.377	-0.093
3	-0.875	0.602	-0.099
4	-1.284	0.798	-0.102
5	-1.568	1.015	-0.102
6	-1.906	1.217	-0.107
7	-2.210	1.359	-0.091

There is so far no compelling theoretical reason to assume that the quasi-normal frequencies should be reflected at the dynamical horizon where the horizon is still evolving. Moreover, we have not accounted for the particular time coordinate and gauge choices made in the numerical simulation. Nevertheless the agreement of $\alpha^{(2)}$ with the QNM damping times can be taken as strong evidence. It would of course be very interesting to find the deeper reasons for why this correspondence happens.

We conclude this section by looking at the vector ξ^a appearing in the flux law of Eq. (22). Fig. 13 shows the integral of $|\xi|^2$ over the MOTS as functions of time. The behavior is very similar to the shear. It turns out to be more difficult to calculate ξ numerically for $\mathcal{H}_{\text{inner}}$ and we shall not do so here. Of greater interest is the behavior for $\mathcal{H}_{\text{outer}}$. Analogous to Eq. (37), we decompose $\xi = \bar{m} \cdot \xi$

using spherical harmonics of spin weight -1 :

$$\bar{\xi}(\theta, \phi, t) = \sum_{l=2}^{\infty} \sum_{m=-l}^l \bar{\xi}_{lm}(t) {}_{-1}Y_{lm}(\theta, \phi). \quad (41)$$

The mode amplitudes are shown in Fig. 14. The behavior is similar to the shear modes, i.e. the initial steep decay followed by shallower decay with oscillations. In principle, one could attempt to compare the decay rates again, this time with the spin-1 perturbations of Schwarzschild. Unfortunately, we are not able to reliably calculate the modes for longer times as we did for the shear (the problem is \hat{r}^a at late times) and thus the best fit values are not reliable either. We shall not pursue this further here.

V. EVOLUTION OF THE MULTIPOLE MOMENTS

Turning now to the multipole moments, before we look at any results and plots, it is clear what we should expect. The situation is very similar to what we have seen for the shear and stability spectrum. First, for the individual horizons \mathcal{S}_1 and \mathcal{S}_2 , we expect at early times to be close to Schwarzschild, i.e. all the higher moments beyond the mass will be small. These will increase as we get closer to the merger, consistent with the increasing energy flux we have encountered in the previous section. Similarly, the common apparent horizon $\mathcal{S}_{\text{outer}}$ should show the opposite behavior, namely large higher moments when it is formed, and settling down to Schwarzschild at later times. The inner horizon $\mathcal{S}_{\text{inner}}$ as usual is expected to be more complex, especially near T_{touch} . These expectations are borne out in Figs. 15, and 16. In Fig. 15, the individual multipoles are shown both as functions of time, and also as functions of the proper distance between \mathcal{S}_1 and \mathcal{S}_2 . For the common horizons, the plot as a function of time shows the usual bifurcation between the inner and outer horizons. It should be kept in mind that in some sense the distinction between $\mathcal{S}_{\text{inner}}$ and $\mathcal{S}_{\text{outer}}$ is artificial. Together they form a common dynamical horizon, and excluding the time of anomalous area increase, the area radius is a valid coordinate for the complete dynamical horizon. To emphasize this, in the second panel of Fig. 16, we plot the multipoles as a function of the area. This shows that indeed nothing unusual occurs at the bifurcation. At late times, when the rate of area increase is very small, a small increase in area represents a large duration of time (we could have taken other quantities, for example, the shear to be a function of area in the previous section). Similarly, we observe that there is no unusual behavior at T_{touch} when the inner horizon develops cusps and then self intersections.

We now turn to the decay of the multipole moments for the outer dynamical horizon. As before, we use the two component model given in Eq. (39) with the early and late time behavior analyzed, respectively, before $t^{(1)} = 4$

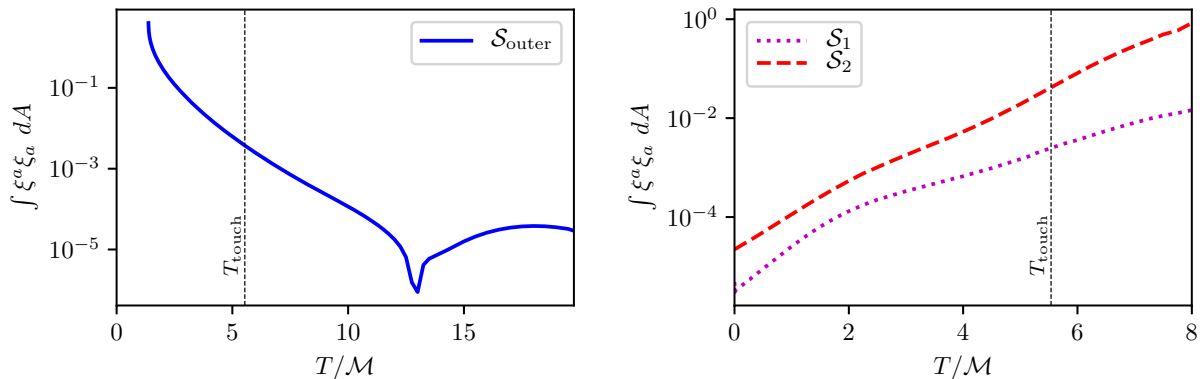


FIG. 13: The behavior of the integral of $|\xi|^2$ for \mathcal{H}_1 , \mathcal{H}_2 and $\mathcal{H}_{\text{outer}}$. The behavior is qualitatively similar to $|\sigma|^2$.

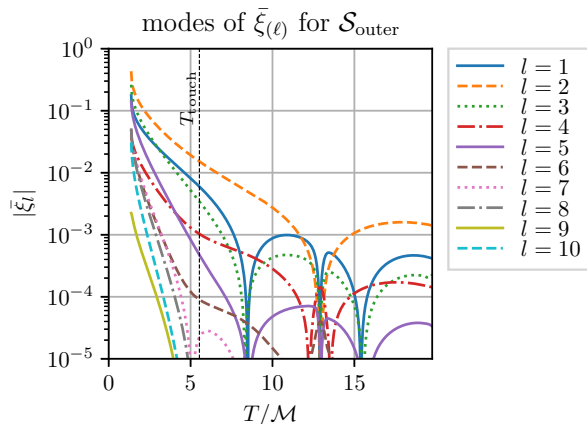


FIG. 14: The mode amplitudes of $\bar{\xi}$ for $\mathcal{H}_{\text{outer}}$ for $l = 1, 2, \dots, 10$. Again the qualitative behavior is similar to the shear modes.

and after $t^{(2)} = 20$. The best fits are shown graphically in Fig. 17. As before, we see clear evidence for the two regimes: a steep initial decay followed by damped oscillations. The best fit values are shown in Table IV. For the late time behavior, we again get good agreement with the fundamental quasinormal mode frequencies and damping times. Again, the case for identifying the early time steep decay with any of the higher overtones is not very convincing.

VI. THE SLOWNESS PARAMETER

We have now seen, from apparently very different perspectives, that we have two distinct post-merger regimes for the outer horizon $\mathcal{H}_{\text{outer}}$. The first is immediately after its formation, at $T_{\text{bifurcate}}$, where we see a rapid approach to equilibrium. Thus, the stability spectrum becomes very close to that of a round 2-sphere, the shear modes and multipoles decay rapidly to zero. This regime is followed by a much slower decay where oscillations in the various fields are easily visible. The decay rates and

TABLE IV: Fits of the multipole moments based on Eqs. (39) and (40) where we chose $T^{(1)} = 4\mathcal{M}$ and $T^{(2)} = 20\mathcal{M}$. For $l < 7$, we estimate the errors of $\Re(\alpha_l^{(2)})$ to be about 1% and of $\Im(\alpha_l^{(2)})$ to be about 10%. All values have been scaled to correspond to a $M_{\text{ADM}} = 1$ simulation.

l	$\alpha_l^{(1)}$	$\Re(\alpha_l^{(2)})$	$\Im(\alpha_l^{(2)})$
2	-0.506	0.377	-0.092
3	-0.854	0.604	-0.098
4	-1.528	0.796	-0.101
5	-1.625	1.017	-0.101
6	-2.008	1.222	-0.108
7	-2.134	1.343	-0.105

oscillations in this slower regime are evidently associated with quasi-normal ringing. The precise transition appears to be a little bit before $10\mathcal{M}$ in simulation time. Since $T_{\text{bifurcate}} \approx 1.37460\mathcal{M}$, this corresponds to $\approx 8\mathcal{M}$ after the common horizon is formed. We note here that this time is quite consistent with observations of the waveform extracted in the wavezone, far away from the black holes [79–83]. In these works it is seen that the gravitational waveform is consistent with the quasi-normal ringing, again beginning at about 8–10 M_{ADM} after the merger (defined variously as the peak of the luminosity or the strain amplitude). Similarly, observational results for the first binary black hole detection also find results consistent with this observation [84].

In this section we would like to speculate about this transition time from the view-point of the horizon dynamics. Is it possible to view this at the time when the black hole transitions from the non-linear to the linear regime? Recent work has argued against such an interpretation [70, 76]. They find that the gravitational wave signal immediately after the merger can be described in terms of the higher overtones of the quasi-normal modes. See also [77, 78]. If this is confirmed, then it indicates that the final black hole can be described perturbatively immediately after its formation. It also makes more promis-

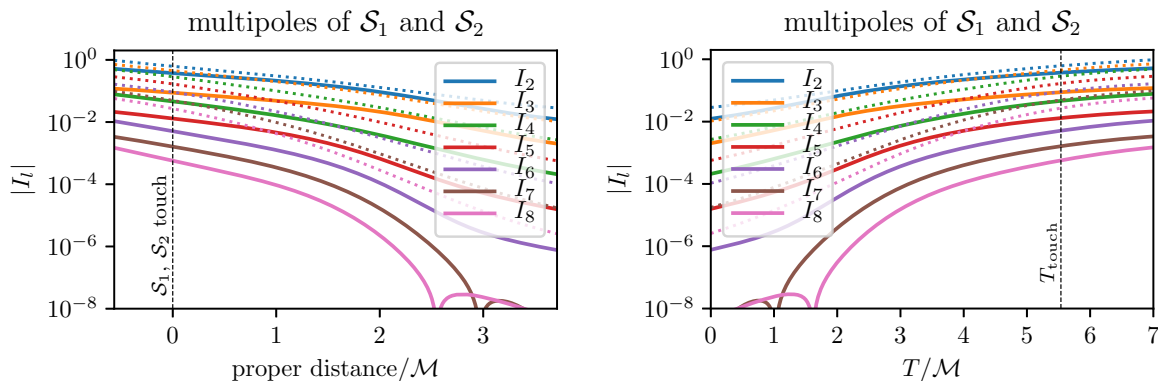


FIG. 15: Multipoles of the two individual horizons as functions of time and separation between the black holes. In each case, the solid line refers to the multipoles of the smaller black hole \mathcal{S}_1 , and the dotted line refers to the larger black hole \mathcal{S}_2 .

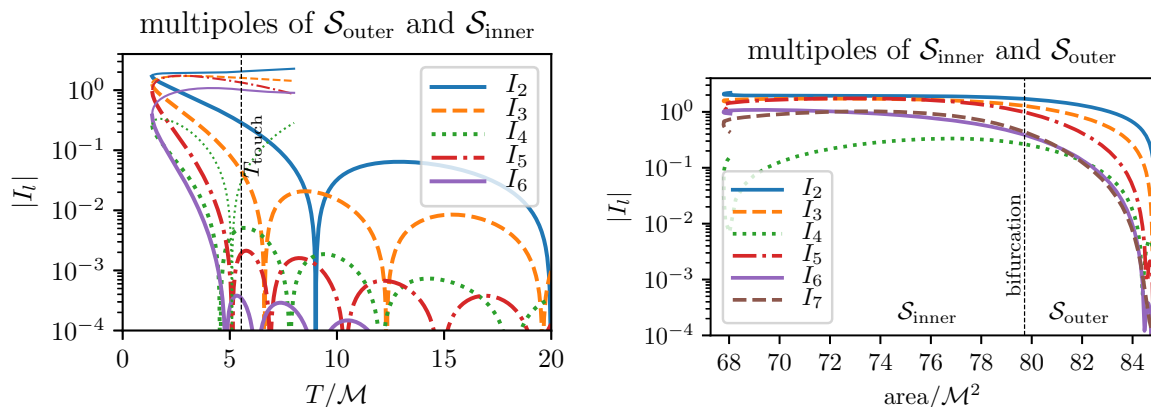


FIG. 16: Multipoles of the inner and outer common horizons as functions of time for $l = 2, 3, \dots, 6$. The left panel shows the moments of the inner and outer horizons as functions of time. The right panel treats the inner and outer MOTSs as forming a single surface with the area as a coordinate.

ing the idea of black hole spectroscopy [85], i.e. observationally testing the black hole no-hair theorem using the ringdown modes [86] (cf. also possible caveats to this in [87]).

Turning now to the properties of $\mathcal{H}_{\text{outer}}$, we have seen that the rapid decay rates immediately after the merger are not consistent with any single higher overtone. This does not rule out the possibility that several modes could be combined to accurately reproduce the decay function that we observe, but we shall not attempt to do so here. Furthermore, even if the immediate post-merger regime is non-perturbative, it does not imply that the quasinormal modes have no role to play: several modes could be present and could be coupled due to non-linear effects. Here we wish to address this question in a different way, namely by looking at evolution equations on $\mathcal{H}_{\text{outer}}$, identifying non-linear terms, and attempting to quantify their importance. We first need to identify which geometric quantities one should consider. In principle, this question is closely tied to the free data on \mathcal{H} , i.e. the

independent geometric fields that must be specified on \mathcal{H} so that we can construct the spacetime in a neighborhood of \mathcal{H} . This has been studied in [44]. As expected, the extrinsic curvatures of each MOTS in the null direction are part of this free data. Our starting point will be an equation we have encountered in paper I, namely the evolution of the expansion $\Theta_{(V)}$ of the time evolution vector V^a in the membrane paradigm interpretation. As in paper I, in terms of the null normals from Eq. (4), the time evolution vector is $V^a = b\ell^a + cn^a$, and the vector orthogonal to $\mathcal{H}_{\text{outer}}$ is $W^a = b\ell^a - cn^a$. We define also $\kappa^{(V)} = -n^b V^a \nabla_a \ell_b$. The qualitative average evolution of the \mathcal{H} can be understood in terms of two dynamical mechanisms simultaneously in place. Each of these mechanisms has an associated time scale. Following [88] which defined a slowness parameter using different timescales (though in a different context), and along the lines in [12, 13], we start from the equation ruling the evolution

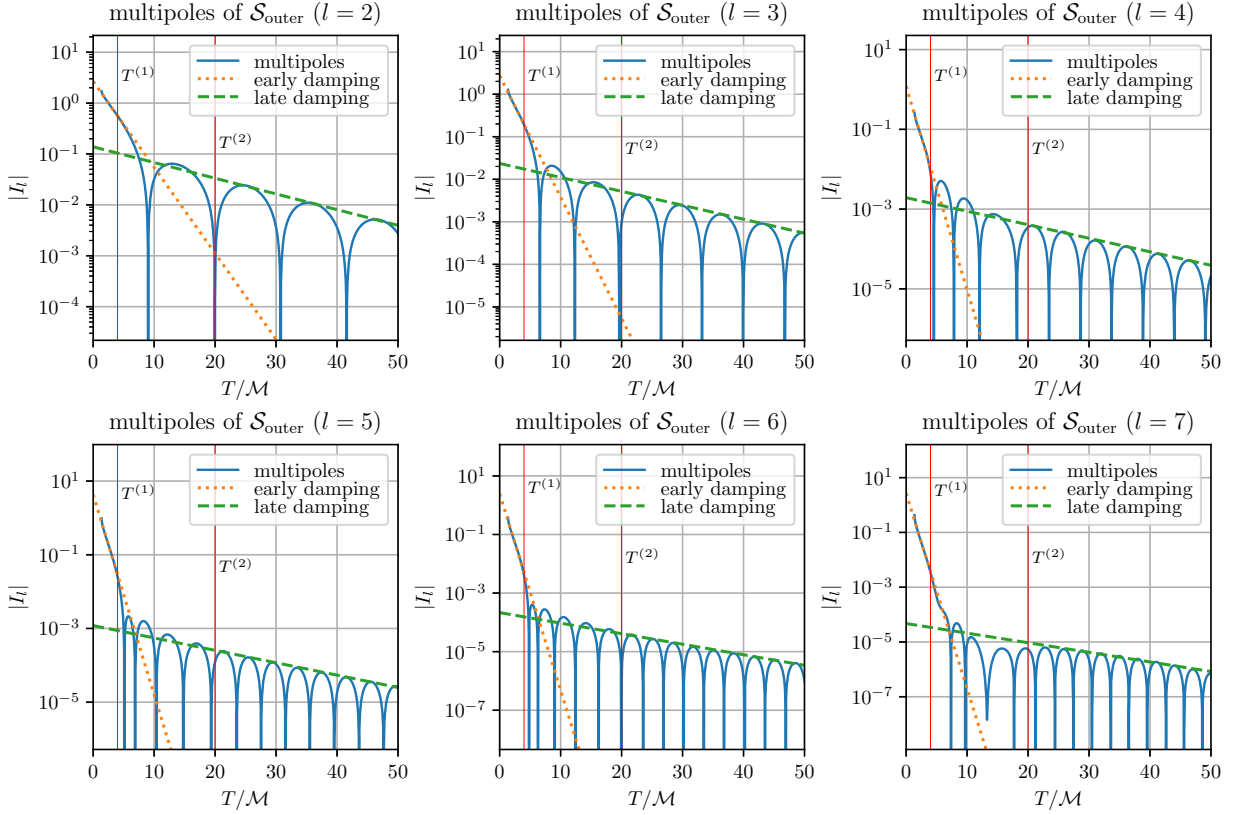


FIG. 17: Fits of the multipole moments for $l = 2, 3, \dots, 7$. The plots are similar to Fig. 12. The blue curves are the multipole moments of the apparent horizon as functions of time, and fits at early and late times are also shown.

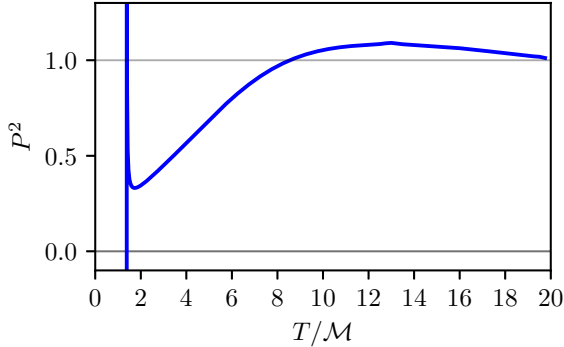


FIG. 18: The slowness parameter as a function of time.

of the expansion $\Theta_{(V)}$ encountered in Sec. VI of paper I:

$$\begin{aligned} \mathcal{L}_V \Theta_{(V)} + \Theta_{(V)}^2 = & -\kappa^{(V)} \Theta_{(V)} + \sigma_{ab}^{(V)} \sigma_{(W)}^{ab} + \frac{1}{2} \Theta_{(V)}^2 \\ & + G_{ab} V^a W^b + (\mathcal{L}_V \ln c) \Theta_{(V)} \\ & + \mathcal{D}^a (c \mathcal{D}_a b - b \mathcal{D}_a c + 2bc \omega_a). \end{aligned} \quad (42)$$

Here G_{ab} is the Einstein tensor. Introducing the notion of a “deformation rate tensor” of \mathcal{S} along V^a (cf. e.g. [5])

$$\Theta_{ab}^{(V)} = \frac{1}{2} q^d{}_a q^d{}_b \mathcal{L}_V q_{cd} = \sigma_{ab}^{(V)} + \frac{1}{2} q_{ab} \Theta^{(V)}, \quad (43)$$

and analogously for W^a , then using $\Theta_{(W)} = -\Theta_{(V)}$, we easily get

$$\Theta_{ab}^{(V)} \Theta_{(W)}^{ab} = \sigma_{ab}^{(V)} \sigma_{(W)}^{ab} - \frac{1}{2} \Theta_{(V)}^2. \quad (44)$$

Eq. (42) can be cast as

$$\begin{aligned} \mathcal{L}_V \Theta_{(V)} = & -\kappa^{(V)} \Theta_{(V)} + \Theta_{ab}^{(V)} \Theta_{(W)}^{ab} \\ & + G_{ab} V^a W^b + (\mathcal{L}_V \ln c) \Theta_{(V)} \\ & + \mathcal{D}^a (c \mathcal{D}_a b - b \mathcal{D}_a c + 2bc \omega_a). \end{aligned} \quad (45)$$

Focusing on the leading terms of the right-hand-side we identify two distinct driving mechanisms: a linear decay term given by the $\kappa^{(V)} \Theta_{(V)}$ and a non-linear term controlled by the deformation rate tensor of the intrinsic geometry of the surface. We expect the linear regime to be characterized by a suppression of strong variations in the area element, and therefore a negligible value of its “acceleration”. This translates into a vanishing of the left hand side in (45) as a signature of linearity. Introducing a “decay timescale” τ as

$$\frac{1}{\tau^2} = \frac{1}{A_S} \oint_S \kappa^{(V)} \Theta_{(V)} dA, \quad (46)$$

and an “oscillation timescale” T controlled by the defor-

mation rate terms

$$\begin{aligned} \frac{1}{T^2} &= \frac{1}{A_S} \oint_S \Theta_{ab}^{(V)} \Theta_{(W)}^{ab} dA \\ &= \frac{1}{A_S} \oint_S \left(\sigma_{ab}^{(V)} \sigma_{(W)}^{ab} - \frac{1}{2} \Theta_{(V)}^2 \right) dA, \end{aligned} \quad (47)$$

we define an instantaneous slowness parameter P [12, 13, 88] as the ratio of the two time scales

$$P = \frac{T}{\tau}. \quad (48)$$

Transition to the linear regime would be marked by the “decay” and “oscillating” terms becoming commensurate and therefore P becoming of order one.

Admittedly, unlike in [88], the identification of the time scales with pure decay and oscillation is not so clear cut here. We have seen that the shear also decays exponentially in time. In any event, regardless of this interpretation, the ratio P captures the ratio of the non-linear to linear term in Eq. (45). When P is close or exceeds unity, then the non-linear term will have a correspondingly smaller effect⁸. It is fairly straightforward to calculate this quantity for $\mathcal{H}_{\text{outer}}$, and the result is shown in Fig. 18. It is clear that early times after the merger, P is small indicating a larger effect of the non-linearities, while it gets close to unity at $\approx 8M$. The non-linear effects thus are not expected to dominate after this time, consistent with our observations of the spectrum, shear, and multipole moments. Appendix D briefly considers the connection between the slowness parameter developed here and the quality factor of a resonator [90]; in particular expressed in terms of quasi-normal mode frequency and damping time [91].

VII. CONCLUSIONS

In this series of two papers we have studied in detail the properties of marginally trapped surfaces in a head-on collision of two non-spinning black holes. Even in this simple and otherwise well studied case, we find interesting geometric and physical behavior. Paper I has considered the status of the area increase law and the associated geometric properties. Here in the second paper, we have studied the stability, the time evolution of fluxes across the horizon and the multipole moments. We have shown that the stability spectrum can be used to obtain

⁸ It is interesting to look at P from the perspective of the fluctuation-dissipation theorem [89] in statistical mechanics. In rough terms, such a theorem states that (crucially, in the linear regime, near equilibrium), the relaxation rate and the fluctuations in a system satisfying a detailed balance are commensurate. In this sense, $P \sim 1$ would mark the transition to a linear regime in which oscillations/(fluctuations) of the system equal its decay rate. Before linearity, there is no reason for this relation to hold.

greater insights into the merger process. We have shown that the decay of fluxes and multipole moments for the final common horizon is consistent with the quasi-normal mode decay time. However, closer to $T_{\text{bifurcate}}$, the time when the common horizon is formed, the decay turns out to be much steeper. This holds for all the modes of the shear and for the various multipole moments as well. The consistency with the quasi-normal mode decay times is not understood from first principles, but it is consistent with the idea of a strong correlation between fields on the horizon and the usual gravitational waveform observed at infinity. We have explored two potential explanations of the faster decay just after $T_{\text{bifurcate}}$. The first is the presence of higher overtones of the fundamental quasi-normal mode, and the second in terms of the slowness parameter. Both of these could potentially explain the behavior. As far as the horizons are concerned, estimates of the decay rates of the shear modes and multipoles favor the slowness parameter.

Future work will consider more generic initial configurations allowing for the black holes to be spinning, and for generic orbits. It should be possible to extend our numerical methods for locating MOTSS to these general situations. This would allow us to tackle interesting questions of interest from both astrophysical and mathematical viewpoints. For example, do the fluxes and multipole moments generically decay at the rate consistent with the quasi-normal modes of the final spinning black hole? Is the early decay consistent with the higher overtones and does the slowness parameter still provide a viable explanation? On the mathematical side, the stability operator becomes non self-adjoint, and the question of stability and zero-crossings of the eigenvalues become much more interesting and complex. This leads to deep connections with the spectral theory of non-self adjoint operators which will be explored in forthcoming work.

ACKNOWLEDGMENTS

We thank Abhay Ashtekar, Ivan Booth and Lamis Al Sheikh for valuable comments and suggestions. Research at Perimeter Institute is supported in part by the Government of Canada through the Department of Innovation, Science and Economic Development Canada and by the Province of Ontario through the Ministry of Colleges and Universities. We also thank the French EIPHI Graduate School (ANR-17-EURE-0002) and the Spanish FIS2017-86497-C2-1 project (with FEDER contribution) for support.

Appendix A: Weyl’s law for large eigenvalues

In this appendix we comment on the universality of the spectrum asymptotics for large Λ_n . In particular, Weyl’s law establishes that the asymptotics of the counting function $N(\Lambda)$ for the Laplacian is determined by geometric

features of \mathcal{S} [61, 92]. Given the compactness of MOTSs, the curvature terms are bounded and do not contribute to the leading behavior, so that

$$N(\Lambda) \sim \frac{A}{4\pi} \Lambda + o(\Lambda), \quad (\Lambda \rightarrow \infty). \quad (\text{A1})$$

In the absence of a boundary the next term in the asymptotic expansion is a constant depending on curvature and corners/cusps [92]. Unfortunately, numerical precision does not allow us to use this to probe the cusp of $\mathcal{S}_{\text{inner}}$ at T_{touch} . Finally, inverting this relation (by naming $n = N(\Lambda_n)$) we get an asymptotic behavior for Λ_n , for large n , namely

$$\Lambda_n \sim \frac{4\pi}{A} n, \quad (n \gg 1). \quad (\text{A2})$$

Appendix B: Perturbative approach for Λ_o of $L^{(-n)}$

Let us introduce an ϵ -dependent operator write $L^{(-n)}(\epsilon)$

$$L^{(-n)}(\epsilon) = -\Delta + \epsilon \mathcal{R}, \quad (\text{B1})$$

so that $L^{(-n)}$ in (9) corresponds to $L^{(-n)}(\frac{1}{2})$. Certainly, $\epsilon = \frac{1}{2}$ is not a small number. But we can explore, without any assumption of spherical symmetry, the time at which $L^{(-n)}$ can be treated as a linear perturbation of the Laplacian (shifted by constant). For this, we consider the eigenvalue problem of the Laplacian

$$-\Delta \phi_l = \Lambda_l^\Delta \phi_l \quad (\text{B2})$$

The Laplacian on the closed surface \mathcal{S} is a self-adjoint non-negative operator with vanishing smallest eigenvalue $\Lambda_o^\Delta = 0$, with constant eigenfunction normalized as $\phi_o = \frac{1}{\sqrt{A}}$. Then, assuming ϵ small, we can perturbatively calculate to the lowest order of the principal eigenvalue of $L^{(-n)}(\epsilon)$ as $\Lambda_o(\epsilon) = \Lambda_o^\Delta + \epsilon \delta \Lambda_o$, with

$$\delta \Lambda_o = \langle \phi_o | \mathcal{R} | \phi_o \rangle = \frac{1}{A} \int_{\mathcal{S}} \mathcal{R} dA = \frac{8\pi}{A}, \quad (\text{B3})$$

where use of the Gauss-Bonnet theorem on a topological sphere has been made. If we now push the perturbative expression (possibly beyond its application range), to $\epsilon = \frac{1}{2}$, we get an estimation of Λ_o for $L^{(-n)}$ as

$$\Lambda_o \sim \frac{4\pi}{A} = \frac{1}{4M_{\text{irr}}^2}, \quad (\text{B4})$$

recovering the expression for $l = 0$ in (24).

Appendix C: A horizon multipoles inequality

To complement the discussion in section V we comment here on an inequality involving horizon mass multipoles. Given the eigenfunctions of the Laplacian spectral

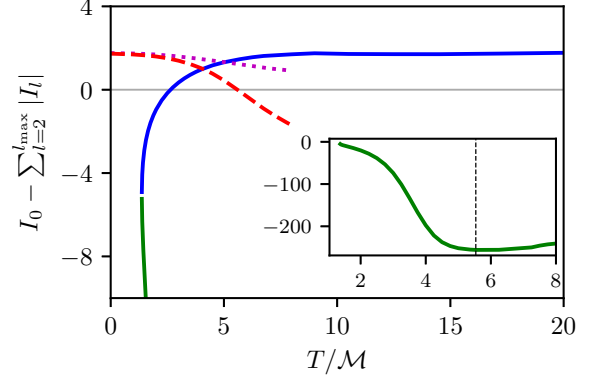


FIG. 19: Multipole inequality for \mathcal{S}_1 , \mathcal{S}_2 , $\mathcal{S}_{\text{inner}}$ and $\mathcal{S}_{\text{outer}}$. We note that the inequality is violated always for $\mathcal{S}_{\text{inner}}$, as it should be. \mathcal{S}_2 and $\mathcal{S}_{\text{outer}}$ also illustrate that the inequality condition is not necessary.

problem (B2), the following result can be derived (details will be given elsewhere):

Proposition. *Given a MOTS \mathcal{S} , where we write $\omega_a = z_a + \mathcal{D}_a \lambda$ with $\mathcal{D}_a z^a = 0$ and Laplacian eigenfunctions ϕ_l are normalized as $\langle \phi_l, \phi_k \rangle = \delta_{lk}$, if the inequality*

$$\sum_{l \neq 0}^{\infty} \left| \int_{\mathcal{S}} \left(\frac{1}{2} \mathcal{R} - z_a z^a - G_{ab} \ell^a n^b \right) (\sqrt{A} \phi_l) dA \right| < \int_{\mathcal{S}} \left(\frac{1}{2} \mathcal{R} - z_a z^a - G_{ab} \ell^a n^b \right) dA \quad (\text{C1})$$

is satisfied, then the MOTS is stable.

In our case vacuum axisymmetric case, and using Gauss-Bonnet this reduces to

$$\sum_{l \neq 0}^{\infty} \left| \int_{\mathcal{S}} \mathcal{R} \phi_l dA \right| < \frac{8\pi}{\sqrt{A}} \implies \text{MOTS stability}, \quad (\text{C2})$$

that provides an inequality in terms of the horizon multipoles introduced in [58]. Therefore, if the MOTS is not highly distorted in the sense that inequality in (C2) is satisfied this provides a sufficient (but not necessary) condition for stability. Perhaps more interestingly, its contraposition states that if the MOTS is unstable then the inequality is violated. Even though, in a strict sense, the result does not apply for the multipoles I_l in section V, the fulfillment of the inequality

$$\sum_{l=2}^{\infty} |I_l| < I_o, \quad (\text{C3})$$

should provide a good estimation for a sufficient condition of MOTS stability, as indeed confirmed in Fig.19.

Appendix D: Black holes as resonators: The quality factor Q and the slowness parameter

If we examine the black hole resulting from a binary merger as a resonator emitting as it is damped towards stationarity, the notion of the slowness parameter P that we have introduced makes contact with the concept of a “quality factor”, or Q-factor, of the resonator. Specifically, given a resonance frequency $\omega_n = \Omega_n - i\frac{\Gamma}{2}$, the quality factor Q_n associated to ω_n is characterized as

$$Q_n = \frac{\Omega_n}{\Gamma} = -\frac{1}{2} \frac{\Re(\omega_n)}{\Im(\omega_n)} \quad (\text{D1})$$

If we introduce, in the linear regime of the dynamics, a decay timescale $\tau_n = 1/|\Im(\omega_n)|$ and an oscillation timescale $T_n = 1/\Re(\omega_n)$ by using the QNM frequencies, then the associated slowness parameter $P_n = T_n/\tau_n = |\Im(\omega_n)|/\Re(\omega_n)$ (cf. [13, 91]) is essentially the inverse of the quality factor $P_n = \frac{1}{2Q_n}$ (this translates into a poor

Q-factor for $l = 2, n = 1$ of $Q \sim 2$ for Schwarzschild). Certainly, the instantaneous $P(t)$ introduced in (48) can be rescaled to match asymptotically a value constructed from the QNM P_n but, in the absence of a sound understanding of the transition to linearity, such adjustment is just ad hoc. More interesting in this association of a Q-factor to the black hole is the definition of Q_n in terms of the ratio of the time-averaged energy stored in the resonator to the energy loss per cycle

$$Q_n = \Omega_n \frac{\text{Stored Energy}}{\text{Power Loss}}. \quad (\text{D2})$$

Given that power loss can be accessed experimentally and that a value of Q_n follows from known QNMs, expression (D2) offers an avenue to assign an energy content to the black hole, associated with a given resonant mode. Interestingly QNM analysis has recently received much attention in the nanoresonator optical community [90], opening a possibility for mutual transfer of tools.

-
- [1] Daniel Pook-Kolb, Ofek Birnholtz, Badri Krishnan, and Erik Schnetter, “Existence and stability of marginally trapped surfaces in black-hole spacetimes,” *Phys. Rev. D* **99**, 064005 (2019).
- [2] Daniel Pook-Kolb, Ofek Birnholtz, Badri Krishnan, and Erik Schnetter, “Self-intersecting marginally outer trapped surfaces,” *Phys. Rev. D* **100**, 084044 (2019).
- [3] Ivan Booth, “Black hole boundaries,” *Can. J. Phys.* **83**, 1073–1099 (2005), arXiv:gr-qc/0508107.
- [4] Abhay Ashtekar and Badri Krishnan, “Isolated and dynamical horizons and their applications,” *Living Rev. Rel.* **7**, 10 (2004), arXiv:gr-qc/0407042.
- [5] Eric Gourgoulhon and Jose Luis Jaramillo, “A 3+1 perspective on null hypersurfaces and isolated horizons,” *Phys. Rept.* **423**, 159–294 (2006), arXiv:gr-qc/0503113.
- [6] Jose Luis Jaramillo, “An introduction to local Black Hole horizons in the 3+1 approach to General Relativity,” *Int. J. Mod. Phys. D* **20**, 2169 (2011), arXiv:1108.2408 [gr-qc].
- [7] Valerio Faraoni and Angus Prain, “Understanding dynamical black hole apparent horizons,” *Lecture Notes in Physics* **907**, 1–199 (2015), arXiv:1511.07775 [gr-qc].
- [8] Matt Visser, “Black holes in general relativity,” *PoS BHS GRANDSTRINGS2008*, 001 (2008), arXiv:0901.4365 [gr-qc].
- [9] Sean A. Hayward, “Black holes: New horizons,” in *Recent developments in theoretical and experimental general relativity, gravitation and relativistic field theories. Proceedings, 9th Marcel Grossmann Meeting, MG’9, Rome, Italy, July 2-8, 2000. Pts. A-C* (2000) pp. 568–580, arXiv:gr-qc/0008071 [gr-qc].
- [10] Abhay Ashtekar and Badri Krishnan, “Dynamical horizons: Energy, angular momentum, fluxes and balance laws,” *Phys. Rev. Lett.* **89**, 261101 (2002), arXiv:gr-qc/0207080.
- [11] Abhay Ashtekar and Badri Krishnan, “Dynamical horizons and their properties,” *Phys. Rev. D* **68**, 104030 (2003), arXiv:gr-qc/0308033.
- [12] Jose Luis Jaramillo, Rodrigo P. Macedo, Philipp Mösta, and Luciano Rezzolla, “Black-hole horizons as probes of black-hole dynamics II: geometrical insights,” *Phys. Rev. D* **85**, 084031 (2012), arXiv:1108.0061 [gr-qc].
- [13] J. L. Jaramillo, R. P. Macedo, P. Mösta, and L. Rezzolla, “Towards a cross-correlation approach to strong-field dynamics in Black Hole spacetimes,” *Proceedings, Spanish Relativity Meeting : Towards new paradigms. (ERE 2011): Madrid, Spain, August 29-September 2, 2011*, AIP Conf. Proc. **1458**, 158–173 (2011), arXiv:1205.3902 [gr-qc].
- [14] Luciano Rezzolla, Rodrigo P. Macedo, and Jose Luis Jaramillo, “Understanding the ‘anti-kick’ in the merger of binary black holes,” *Phys. Rev. Lett.* **104**, 221101 (2010), arXiv:1003.0873 [gr-qc].
- [15] Anshu Gupta, Badri Krishnan, Alex Nielsen, and Erik Schnetter, “Dynamics of marginally trapped surfaces in a binary black hole merger: Growth and approach to equilibrium,” *Phys. Rev. D* **97**, 084028 (2018), arXiv:1801.07048 [gr-qc].
- [16] Vaishak Prasad, Anshu Gupta, Sukanta Bose, Badri Krishnan, and Erik Schnetter, “News from horizons in binary black hole mergers,” (2020), arXiv:2003.06215 [gr-qc].
- [17] José Luis Jaramillo, “A Young-Laplace law for black hole horizons,” *Phys. Rev. D* **89**, 021502 (2014), arXiv:1309.6593 [gr-qc].
- [18] José Luis Jaramillo, “Black hole horizons and quantum charged particles,” *Class. Quant. Grav.* **32**, 132001 (2015), arXiv:1410.0509 [gr-qc].
- [19] Jos Luis Jaramillo, “A perspective on Black Hole Horizons from the Quantum Charged Particle,” *Proceedings, Spanish Relativity Meeting: Almost 100 years after Einstein Revolution (ERE 2014): Valencia, Spain, September 1-5, 2014*, J. Phys. Conf. Ser. **600**, 012037 (2015), arXiv:1608.05963 [gr-qc].
- [20] Abhay Ashtekar, Christopher Beetle, and Jerzy Lewandowski, “Mechanics of Rotating Isolated Hori-

- zons,” *Phys. Rev.* **D64**, 044016 (2001), arXiv:gr-qc/0103026.
- [21] Daniel Pook-Kolb, Ofek Birnholtz, Badri Krishnan, and Erik Schnetter, “MOTS Finder version 1.1,” (2019), 10.5281/zenodo.2591105.
- [22] Jonathan Thornburg, “A Fast Apparent-Horizon Finder for 3-Dimensional Cartesian Grids in Numerical Relativity,” *Class. Quant. Grav.* **21**, 743–766 (2004), arXiv:gr-qc/0306056.
- [23] Jonathan Thornburg, “Event and Apparent Horizon Finders for 3 + 1 Numerical Relativity,” *Living Rev. Rel.* **10**, 3 (2007), arXiv:gr-qc/0512169.
- [24] Jonathan Thornburg, “Finding apparent horizons in numerical relativity,” *Phys. Rev. D* **54**, 4899–4918 (1996), arXiv:gr-qc/9508014.
- [25] Deirdre M. Shoemaker, Mijan F. Huq, and Richard A. Matzner, “Generic Tracking of Multiple Apparent Horizons with Level Flow,” *Phys. Rev.* **D62**, 124005 (2000), arXiv:gr-qc/0004062.
- [26] Lap-Ming Lin and Jerome Novak, “A new spectral apparent horizon finder for 3D numerical relativity,” *Class. Quant. Grav.* **24**, 2665–2676 (2007), arXiv:gr-qc/0702038.
- [27] Frank Löffler, Joshua Faber, Eloisa Bentivegna, Tanja Bode, Peter Diener, Roland Haas, Ian Hinder, Bruno C. Mundim, Christian D. Ott, Erik Schnetter, Gabrielle Allen, Manuela Campanelli, and Pablo Laguna, “The Einstein Toolkit: A Community Computational Infrastructure for Relativistic Astrophysics,” *Class. Quantum Grav.* **29**, 115001 (2012), arXiv:1111.3344 [gr-qc].
- [28] EinsteinToolkit, “Einstein Toolkit: Open software for relativistic astrophysics,” <http://einstein toolkit.org/>.
- [29] Marcus Ansorg, Bernd Brügmann, and Wolfgang Tichy, “A single-domain spectral method for black hole puncture data,” *Phys. Rev. D* **70**, 064011 (2004), arXiv:gr-qc/0404056.
- [30] J. David Brown, Peter Diener, Olivier Sarbach, Erik Schnetter, and Manuel Tiglio, “Turduckening black holes: an analytical and computational study,” *Phys. Rev. D* **79**, 044023 (2009), arXiv:0809.3533 [gr-qc].
- [31] Sascha Husa, Ian Hinder, and Christiane Lechner, “Kranc: a Mathematica application to generate numerical codes for tensorial evolution equations,” *Comput. Phys. Commun.* **174**, 983–1004 (2006), arXiv:gr-qc/0404023.
- [32] Kranc, “Kranc: Kranc assembles numerical code,” .
- [33] Dieter R. Brill and Richard W. Lindquist, “Interaction energy in geometrostatics,” *Phys. Rev.* **131**, 471–476 (1963).
- [34] S.A. Hayward, “General laws of black hole dynamics,” *Phys.Rev.* **D49**, 6467–6474 (1994).
- [35] Abhay Ashtekar, Christopher Beetle, and Stephen Fairhurst, “Isolated horizons: A generalization of black hole mechanics,” *Class. Quant. Grav.* **16**, L1–L7 (1999), arXiv:gr-qc/9812065.
- [36] Abhay Ashtekar, Christopher Beetle, and Stephen Fairhurst, “Mechanics of Isolated Horizons,” *Class. Quant. Grav.* **17**, 253–298 (2000), arXiv:gr-qc/9907068.
- [37] Abhay Ashtekar, Christopher Beetle, and Jerzy Lewandowski, “Geometry of Generic Isolated Horizons,” *Class. Quant. Grav.* **19**, 1195–1225 (2002), arXiv:gr-qc/0111067.
- [38] Jerzy Lewandowski, “Spacetimes Admitting Isolated Horizons,” *Class. Quant. Grav.* **17**, L53–L59 (2000), arXiv:gr-qc/9907058.
- [39] Jerzy Lewandowski and Carmen Li, “Spacetime near Kerr isolated horizon,” (2018), arXiv:1809.04715 [gr-qc].
- [40] Mikolaj Korzynski, Jerzy Lewandowski, and Tomasz Pawłowski, “Mechanics of multidimensional isolated horizons,” *Class. Quant. Grav.* **22**, 2001–2016 (2005), arXiv:gr-qc/0412108.
- [41] Abhay Ashtekar, Stephen Fairhurst, and Badri Krishnan, “Isolated horizons: Hamiltonian evolution and the first law,” *Phys. Rev.* **D62**, 104025 (2000), arXiv:gr-qc/0005083.
- [42] Badri Krishnan, “The spacetime in the neighborhood of a general isolated black hole,” *Class.Quant.Grav.* **29**, 205006 (2012), arXiv:1204.4345 [gr-qc].
- [43] Ivan S. Booth, “Metric-based Hamiltonians, null boundaries, and isolated horizons,” *Class. Quant. Grav.* **18**, 4239–4264 (2001), arXiv:gr-qc/0105009.
- [44] Ivan Booth, “Spacetime near isolated and dynamical trapping horizons,” *Phys. Rev. D* **87**, 024008 (2013), arXiv:1207.6955 [gr-qc].
- [45] Olaf Dreyer, Badri Krishnan, Deirdre Shoemaker, and Erik Schnetter, “Introduction to Isolated Horizons in Numerical Relativity,” *Phys. Rev.* **D67**, 024018 (2003), arXiv:gr-qc/0206008.
- [46] Lars Andersson, Marc Mars, and Walter Simon, “Local existence of dynamical and trapping horizons,” *Phys.Rev.Lett.* **95**, 111102 (2005), arXiv:gr-qc/0506013 [gr-qc].
- [47] Lars Andersson, Marc Mars, and Walter Simon, “Stability of marginally outer trapped surfaces and existence of marginally outer trapped tubes,” *Adv.Theor.Math.Phys.* **12** (2008), arXiv:0704.2889 [gr-qc].
- [48] Ivan Booth and Stephen Fairhurst, “Isolated, slowly evolving, and dynamical trapping horizons: geometry and mechanics from surface deformations,” *Phys. Rev.* **D75**, 084019 (2007), arXiv:gr-qc/0610032.
- [49] R.P.A.C. Newman, “Topology and stability of marginal 2-surfaces,” *Class. and Quant. Grav.* **4**, 277–290 (1987).
- [50] Abhay Ashtekar, Jonathan Engle, Tomasz Pawłowski, and Chris Van Den Broeck, “Multipole moments of isolated horizons,” *Class. Quant. Grav.* **21**, 2549–2570 (2004), arXiv:gr-qc/0401114.
- [51] Abhay Ashtekar, Miguel Campiglia, and Samir Shah, “Dynamical Black Holes: Approach to the Final State,” *Phys. Rev.* **D88**, 064045 (2013), arXiv:1306.5697 [gr-qc].
- [52] S. W. Hawking and J. B. Hartle, “Energy and angular momentum flow into a black hole,” *Commun. Math. Phys.* **27**, 283–290 (1972).
- [53] Ivan Booth and Stephen Fairhurst, “The first law for slowly evolving horizons,” *Phys. Rev. Lett.* **92**, 011102 (2004), arXiv:gr-qc/0307087.
- [54] Stephen O’Sullivan and Scott A. Hughes, “Strong-field tidal distortions of rotating black holes: Formalism and results for circular, equatorial orbits,” *Phys. Rev. D* **90**, 124039 (2014), [Erratum: *Phys.Rev.D* 91, 109901 (2015)], arXiv:1407.6983 [gr-qc].
- [55] Stephen O’Sullivan and Scott A. Hughes, “Strong-field tidal distortions of rotating black holes: II. Horizon dynamics from eccentric and inclined orbits,” *Phys. Rev. D* **94**, 044057 (2016), arXiv:1505.03809 [gr-qc].
- [56] Robert P. Geroch, “Multipole moments. II. Curved space,” *J. Math. Phys.* **11**, 2580–2588 (1970).
- [57] R. O. Hansen, “Multipole moments of stationary spacetimes,” *J. Math. Phys.* **15**, 46–52 (1974).

- [58] Robert Owen, “The Final Remnant of Binary Black Hole Mergers: Multipolar Analysis,” *Phys. Rev.* **D80**, 084012 (2009), arXiv:0907.0280 [gr-qc].
- [59] Lieb E.H. and Thirring W.E., “Inequalities for the moments of the eigenvalues of the schrodinger hamiltonian and their relation to sobolev inequalities,” in *The Stability of Matter: From Atoms to Stars*, edited by Thirring W.E. (Springer, Berlin, Heidelberg, 1991) p. 269.
- [60] M. Berry, “Semiclassical mechanics of regular and irregular motion,” in *Comportement chaotique des systèmes déterministes*, Les Houches, session XXXVI, edited by G. Iooss, R. H. G. Helleman, and R. Stora (1981) north-holland ed., pp. 173–271.
- [61] Marcel Berger, *A panoramic view of Riemannian geometry* (Springer, Berlin, 2003).
- [62] Oriol Bohigas, Marie-Joya Giannoni, and Charles Schmit, “Spectral fluctuations of classically chaotic quantum systems,” in *Quantum chaos and statistical nuclear physics* (Springer, 1986) pp. 18–40.
- [63] M.V. Berry, I.C. Percival, and N.O. Weiss, “Quantum chaology,” *Proc. Roy. Soc. London A* **413**, 183–198 (1987).
- [64] Bruno Eckhardt, “Quantum mechanics of classically non-integrable systems,” *Physics Reports* **163**, 205 – 297 (1988).
- [65] Sandro Wimberger, *Nonlinear Dynamics and Quantum Chaos* (Springer International Publishing, Switzerland, 2014).
- [66] C.E. Porter, *Statistical Theories of Spectra: Fluctuations : a Collection of Reprints and Original Papers*, Perspectives in physics : A series of reprint collections (Acad. Press, 1965).
- [67] Freeman J Dyson, “Statistical theory of the energy levels of complex systems. i,” *Journal of Mathematical Physics* **3**, 140–156 (1962).
- [68] Freeman J Dyson, “Statistical theory of the energy levels of complex systems. ii,” *Journal of Mathematical Physics* **3**, 157–165 (1962).
- [69] Freeman J Dyson, “Statistical theory of the energy levels of complex systems. iii,” *Journal of Mathematical Physics* **3**, 166–175 (1962).
- [70] Matthew Giesler, Maximiliano Isi, Mark A. Scheel, and Saul Teukolsky, “Black Hole Ringdown: The Importance of Overtones,” *Phys. Rev. X* **9**, 041060 (2019), arXiv:1903.08284 [gr-qc].
- [71] C.V. Vishveshwara, “Scattering of Gravitational Radiation by a Schwarzschild Black-hole,” *Nature* **227**, 936–938 (1970).
- [72] S. Chandrasekhar and Steven L. Detweiler, “The quasinormal modes of the Schwarzschild black hole,” *Proc. Roy. Soc. Lond. A* **A344**, 441–452 (1975).
- [73] E Berti, ”<https://pages.jh.edu/~eberti2/ringdown/>”.
- [74] Emanuele Berti, Vitor Cardoso, and Andrei O. Starinets, “Quasinormal modes of black holes and black branes,” *Class. Quant. Grav.* **26**, 163001 (2009), arXiv:0905.2975 [gr-qc].
- [75] Emanuele Berti, Vitor Cardoso, and Clifford M. Will, “On gravitational-wave spectroscopy of massive black holes with the space interferometer LISA,” *Phys. Rev. D* **73**, 064030 (2006), arXiv:gr-qc/0512160.
- [76] Maria Okounkova, “Revisiting non-linearity in binary black hole mergers,” (2020), arXiv:2004.00671 [gr-qc].
- [77] Xisco Jimnez Forteza, Swetha Bhagwat, Paolo Pani, and Valeria Ferrari, “On the spectroscopy of binary black hole ringdown using overtones and angular modes,” (2020), arXiv:2005.03260 [gr-qc].
- [78] Swetha Bhagwat, Xisco Jimenez Forteza, Paolo Pani, and Valeria Ferrari, “Ringdown overtones, black hole spectroscopy, and no-hair theorem tests,” *Phys. Rev. D* **101**, 044033 (2020), arXiv:1910.08708 [gr-qc].
- [79] Ioannis Kamaretsos, Mark Hannam, Sascha Husa, and B. S. Sathyaprakash, “Black-hole hair loss: learning about binary progenitors from ringdown signals,” *Phys. Rev.* **D85**, 024018 (2012), arXiv:1107.0854 [gr-qc].
- [80] Ioannis Kamaretsos, Mark Hannam, and B. Sathyaprakash, “Is black-hole ringdown a memory of its progenitor?” *Phys. Rev. Lett.* **109**, 141102 (2012), arXiv:1207.0399 [gr-qc].
- [81] Swetha Bhagwat, Maria Okounkova, Stefan W. Ballmer, Duncan A. Brown, Matthew Giesler, Mark A. Scheel, and Saul A. Teukolsky, “On choosing the start time of binary black hole ringdowns,” *Phys. Rev.* **D97**, 104065 (2018), arXiv:1711.00926 [gr-qc].
- [82] S. Borhanian, K.G. Arun, H.P. Pfeiffer, and B.S. Sathyaprakash, “Comparison of post-Newtonian mode amplitudes with numerical relativity simulations of binary black holes,” *Class. Quant. Grav.* **37**, 065006 (2020).
- [83] Ssohrab Borhanian, K. G. Arun, Harald P. Pfeiffer, and B. S. Sathyaprakash, “Signature of horizon dynamics in binary black hole gravitational waveforms,” (2019), arXiv:1901.08516 [gr-qc].
- [84] B. P. Abbott *et al.* (Virgo, LIGO Scientific), “Tests of general relativity with GW150914,” *Phys. Rev. Lett.* **116**, 221101 (2016), arXiv:1602.03841 [gr-qc].
- [85] Olaf Dreyer, Bernard J. Kelly, Badri Krishnan, Lee Samuel Finn, David Garrison, and Ramon Lopez-Aleman, “Black hole spectroscopy: Testing general relativity through gravitational wave observations,” *Class. Quant. Grav.* **21**, 787–804 (2004), arXiv:gr-qc/0309007 [gr-qc].
- [86] Maximiliano Isi, Matthew Giesler, Will M. Farr, Mark A. Scheel, and Saul A. Teukolsky, “Testing the no-hair theorem with GW150914,” *Phys. Rev. Lett.* **123**, 111102 (2019), arXiv:1905.00869 [gr-qc].
- [87] José Luis Jaramillo, Rodrigo Panosso Macedo, and Lamis Al Sheikh, “Pseudospectrum and black hole quasinormal mode (in)stability,” (2020), arXiv:2004.06434 [gr-qc].
- [88] Richard H. Price, Gaurav Khanna, and Scott A. Hughes, “Systematics of black hole binary inspiral kicks and the slowness approximation,” *Phys.Rev.* **D83**, 124002 (2011), arXiv:1104.0387 [gr-qc].
- [89] R Kubo, “The fluctuation-dissipation theorem,” *Reports on Progress in Physics* **29**, 255–284 (1966).
- [90] Lalanne Philippe, Yan Wei, Vynck Kevin, Sauvan Christophe, and Hugonin JeanPaul, “Light interaction with photonic and plasmonic resonances,” *Laser & Photonics Reviews* **12**, 1700113 (2018), <https://onlinelibrary.wiley.com/doi/pdf/10.1002/lpor.201700113>.
- [91] Jose Luis Jaramillo, Rodrigo Panosso Macedo, Philipp Mösta, and Luciano Rezzolla, “Black-hole horizons as probes of black-hole dynamics I: post-merger recoil in head-on collisions,” *Phys.Rev.* **D85**, 084030 (2012), arXiv:1108.0060 [gr-qc].
- [92] Heinrich P Baltés and Eberhard R Hilf, *Spectra of finite systems* (BI-Wissenschaftsverlag Mannheim, 1976).